

Empirical Evidence for the Frontal Modification of Atmospheric Boundary Layer Depth Variability over Land

NICHOLAS E. CLARK,^{a,b} SANDIP PAL,^a AND TEMPLE R. LEE^c

^a *Department of Geosciences, Atmospheric Science Division, Texas Tech University, Lubbock, Texas*

^b *Honors College, Texas Tech University, Lubbock, Texas*

^c *NOAA/Air Resources Laboratory Atmospheric Turbulence and Diffusion Division, Oak Ridge, Tennessee*

(Manuscript received 25 May 2021, in final form 4 April 2022)

ABSTRACT: Despite many observational studies on the atmospheric boundary layer (ABL) depth z_i variability across various time scales (e.g., diurnal, seasonal, annual, and decadal), z_i variability before, during, and after frontal passages over land, or simply z_i variability as a function of weather patterns, has remained relatively unexplored. In this study, we provide an empirical framework using 5 years (2014–18) of daytime rawinsonde observations and surface analyses over 18 central and southeastern U.S. sites to report z_i variability across frontal boundaries. By providing systematic observations of front-relative contrasts in z_i (i.e., z_i differences between warm and cold sectors, $\Delta z_i = z_i^{\text{Warm}} - z_i^{\text{Cold}}$) and boundary layer moisture (i.e., ABL- q) regimes in summer and winter, we propose a new paradigm to study z_i changes across cold-frontal boundaries. For most cases, we found deeper z_i over the warm sector than the cold sector in both summer and winter, although with significant site-to-site variability in Δz_i . Additionally, our results show a positive Δq_{ABL} (i.e., frontal contrasts in ABL- q) in summer and winter, supporting what is typically observed in midlatitude cyclones. We found that a front-relative Δq_{ABL} of 1 g kg^{-1} often yielded at least a 100-m Δz_i across the frontal boundary in both summer and winter. This work provides a synoptic-scale basis for z_i variability and establishes a foundation for model verification to examine the impact of air mass exchange associated with advection on z_i . This work will advance our understanding of ABL processes in synoptic environments and help unravel sources of front-relative z_i variability.

SIGNIFICANCE STATEMENT: The atmospheric boundary layer (ABL) is the lowermost part of the atmosphere adjacent to Earth's surface. The irregular motion of air inside the ABL plays an essential role in relocating air near the surface to the free troposphere. Meteorologists use ABL depth in weather forecast models to determine the atmosphere's ability to dilute or enrich tracers within the ABL. However, knowledge about the changes in ABL depth during stormy conditions remains incomplete. Here, we investigate how the ABL depth varies before and after cold-frontal passages. We found that ABL depths were much deeper before the cold-frontal passages than after. This knowledge will help us develop new approaches to consider how storms modify the ABL in weather forecast models.


KEYWORDS: Atmosphere; North America; Advection; Synoptic climatology; Boundary layer; Temperature; Water vapor; Radiosonde/rawinsonde observations; Seasonal variability

1. Introduction

Midlatitude cyclones and associated passages of cold and warm fronts over the land surface often lead to high-impact weather events (i.e., deep moist convection, damaging winds, and extreme precipitation) and affect continental transport processes of tracers (e.g., Browning et al. 1973; Winkler et al. 1988; Boutle et al. 2011; Pal et al. 2020a). The sequential passages of low pressure (cyclonic) and high pressure (anticyclonic) systems over a particular location trigger a transition of air masses (Stull 1988; Sinclair et al. 2008; Markowski and Richardson 2010) that affects the thermodynamic properties and tracer variability in the atmospheric boundary layer (ABL) and overlying free troposphere (FT). Past studies have shown that frontal passages can prompt the vertical transport

of air masses within the ABL into the lower and upper FT due to frontal lifting mechanisms (e.g., Bethan et al. 1998; Purvis et al. 2003; Wei et al. 2011) and the horizontal transport of pollutants and tracers through the warm conveyor belt in midlatitude cyclones (e.g., Cooper et al. 2004).

There is a strong need to better understand and document the interaction between the ABL and synoptic-scale weather systems (i.e., a cold-frontal passage in this context) in order to improve numerical weather prediction (NWP) models. An improved understanding of this interaction may lead to better parameterizations of temperature and moisture exchange near fronts and better representations of advection of these quantities in NWP models. In their pioneering work on this topic, Lenschow (1973) and Stull (1976) identified that advection can significantly change the ABL environment and that neglecting the impact of advection can potentially cause forecast errors in ABL depths (henceforth referred to as z_i). Thus, in order to drive new-generation measurement and numerical simulation efforts to the next level of accuracy and precision, we need to address the role of advection on z_i changes as this represents a significant gap limiting our understanding,

 Denotes content that is immediately available upon publication as open access.

Corresponding author: Sandip Pal, sandip.pal@ttu.edu

DOI: 10.1175/JAMC-D-21-0099.1

© 2022 American Meteorological Society. For information regarding reuse of this content and general copyright information, consult the [AMS Copyright Policy](#) ([www.ametsoc.org/PUBSReuseLicenses](#)).

simulation, and prediction of ABL processes (e.g., [LeMone et al. 2019](#); [National Academies of Sciences, Engineering, and Medicine 2018](#)).

In general, three competitive forcings govern the ABL development or z_i growth rate (i.e., dz_i/dt) during the entire diurnal cycle, namely, entrainment velocity w_e , mean large-scale vertical motion or subsidence w_s acting at the ABL top, and horizontal advection of state variables by the mean wind ([Stull 1988](#)). Many empirical studies have reported z_i variability on multiple time scales (e.g., diurnal, seasonal, annual, interannual, and decadal) with a critical focus on the first two factors (i.e., w_e and w_s) under the assumption of horizontally homogeneous atmospheric conditions (see reviews on this topic by [Wilczak et al. 1996](#); [Seibert et al. 2000](#); [Engelbart et al. 2007](#); [Emeis et al. 2007](#); [Pal 2014](#); [Barlow 2014](#)). Horizontally inhomogeneous conditions, diverse landscapes, and synoptic weather conditions are well known to trigger flow regimes dominated by advection that further cause empirical findings on z_i variability to be either inappropriately interpreted or oversimplified.

The strength of the thermal advection is determined by the initial baroclinicity and the meridional displacement of air parcels by the cyclone and anticyclone ([Sinclair et al. 2010](#)). Despite the challenges involved in creating a systematic identification of frontal passages over multiple sites, easily accessible and archived synoptic charts provide an excellent opportunity to investigate frontal passages and their impact on ABL thermodynamics. Many climatological studies and model-based investigations have focused on frontal passages at the surface and in the ABL over diverse geographical regions (e.g., [Davis and Kalkstein 1990](#); [Hoch and Markowski 2005](#); [Payer et al. 2011](#); [Shafer and Steenburgh 2008](#); [Berry et al. 2011](#); [Pal et al. 2020a](#)).

Some studies have investigated the impact of frontal passages on the overall ABL thermodynamics over both land and ocean. Based on a Eulerian mass budget approach, [Sinclair et al. \(2010\)](#) discovered a more turbulent ABL regime in the cold sector than in the warm sector of a frontal passage over the Atlantic Europe (i.e., the western portion of Europe that borders the Atlantic Ocean) and claimed that the thermal advection determined the characteristics of the synoptically active ABL. While investigating multiscale observations for a cold-frontal passage, [Harvey et al. \(2017\)](#) found discrepancies between numerical simulations and observations in turbulent fluxes associated with subgrid-scale shear-driven turbulence in the warm sector and consistencies in the turbulent fluxes of ABL moisture and momentum in the cold sector of the front.

Similarly, [Naud et al. \(2016\)](#) found that the ABL structure and its relationship with cloud cover were relatively independent of the large-scale conditions. [Ilotoviz et al. \(2021\)](#) found substantial impacts of dry intrusion on the marine boundary layer (MBL) and cloud structures in the cold sector of trailing fronts, which modified the MBL thermodynamics. Overall, these studies demonstrate the complexity in the thermodynamic behavior of the ABL under the impact of a frontal passage that could be used to further improve NWP models.

To fully understand the impact of midlatitude cyclones on ABL characteristics, a comparative analysis before and after

frontal passages is necessary. For instance, a study conducted by [Bond and Fleagle \(1988\)](#) provided details on pre- versus postfrontal ABL processes for North Pacific storms, reporting larger w_e in postfrontal than prefrontal conditions. Similar results were reported in a more recent field campaign [Fronts and Atlantic Storm Track Experiment (FASTEX)] in [Persson et al. \(2005\)](#). Based on a case study in a high latitude region (i.e., the Helsinki Test bed), [Sinclair et al. \(2012\)](#) reported a deeper ABL in the warm sector followed by a shallower ABL in the cold sector of a nocturnal front, attributing the deeper ABL in the warm sector to shear-driven turbulent mixing.

Most of the studies reported the ABL thermodynamic structures 1) for the MBL (e.g., [Sinclair et al. 2010](#)), 2) within a case study (e.g., [Boutle et al. 2011](#)), 3) for a limited geographic region (e.g., [Sinclair 2013](#)), 4) using observations and reanalyses (e.g., [Shafer and Steenburgh 2008](#)), or 5) by selecting unique nocturnal ABL regimes ([Sinclair et al. 2012](#)). However, there exists limited observations of the ABL thermodynamic structure while under the impact of a frontal passage for a large geographic region on land. Since the diurnal cycle of the ABL features typically fluctuate more substantially over land than over the ocean, the ABL structure over land will have significantly more variability. For example, [Koffi et al. \(2016\)](#) showed ABL diurnal amplitudes to vary (seasonally and spatially) from 500 to 2000 m over multiple sites in Europe. In contrast, [Wulfmeyer and Janjić \(2005\)](#) reported a low diurnal amplitude of MBL depths (~250 m) over the tropical Pacific and did not find any correlation between the MBL depth and the sensible heat and buoyancy fluxes. These findings contrast with regard to the ABL features over land, where mostly strong correlations between z_i and heat fluxes are observed ([Yi et al. 2001](#); [Pal and Haeffelin 2015](#); [Lee et al. 2015](#); [Lopez-Coto et al. 2020](#)). The ABL over land often exhibits a higher amount of variability than the ABL over the ocean, and more observations are necessary to accurately represent the ABL over land in NWP models. An overview of the factors controlling z_i on different temporal and spatial scales can be found in [Medeiros et al. \(2005\)](#).

In summary, there exist no systematic analyses on the effects of frontal passages on z_i variability over land during two contrasting seasons. Additionally, an empirical investigation will provide the opportunity to improve NWP models with varying spatiotemporal resolutions to simulate front-relative z_i features [e.g., North American Model (NAM), [Janjic and Gall 2012](#); High-Resolution Rapid Refresh (HRRR), [Benjamin et al. 2016](#); and Global Transport Model, [Koffi et al. 2016](#)].

Based on previous studies, we hypothesize that during quasi-periodic passages of cyclonic and anticyclonic flows, the ABL encounters vigorous changes (both vertically and horizontally) due to the possible air mass exchange associated with the frontal passage, perturbed land surface forcing via changes in soil moisture regimes due to precipitation, subsidence over the high-pressure-dominated cold sector, and cloud coverage and frontal lifting in the vicinity of the frontal boundary. We focus on the frontal modification of ABL dynamics using routine observations, specifically to 1) understand the front-relative changes in daytime z_i so that a comparison between z_i in warm (also referred to as prefrontal) versus cold

(postfrontal) sectors, which we term Δz_i , can be elucidated; 2) investigate the Δz_i during summer and winter to understand how the frontal impact on z_i varies between two contrasting seasons; 3) determine how Δz_i changes spatially; and 4) diagnose frontal-regimes and cyclone tracks when Δz_i may be linked to the impact of contrasting meteorological processes occurring in the warm and cold sectors.

2. Experimental region and datasets

To address the research goals, we used five years (from 1 December 2013 through 31 December 2018) of rawinsonde observations over 18 sites in the central and southeast United States and surface map analyses for each site (Fig. 1; Table A1 in appendix A). The characteristics of synoptic fronts over the experimental region are mainly governed by the typical mid-latitude cyclone tracks (Davis et al. 1997). In general, frontal passages associated with midlatitude cyclones in the continental United States separate polar or arctic air from the more humid tropical air that originates in Canada (cold-sector flow) and the Gulf of Mexico (warm-sector flow), respectively (e.g., Neiman et al. 1998). The majority of the extratropical cyclones move eastward across the United States, yielding a north-northwesterly and south-southeasterly flow in the cold and warm sectors, respectively. This exchange between air masses leads to significant weather events across central and northeastern United States (e.g., Dolan and Davis 1992). The southern extension of these frontal passages is often impeded by a semi-permanent high pressure system located over the North Atlantic basin (e.g., Wang et al. 2016), particularly in summer (Parsons et al. 1991). Thus, the frequency of fronts is greater in the central and northeastern United States than in the southern United States (e.g., Davis et al. 1997). Additionally, during spring and early summer, drylines also form in the mid-western United States between maritime (moist) and continental (hot and dry) air masses that pass over arid regions and subside in the lee of the Rocky Mountains, in particular over the west Texas region (Hoch and Markowski 2005).

While selecting the Integrated Global Radiosonde Archive (IGRA) sites, we confirmed that the ABL measurements at the locations were not affected by the inflow of the urban boundary layer (UBL) (i.e., IGRA sites near metropolitan areas), excluding stations such as Minneapolis, Minnesota (KMPX), and Dallas–Fort Worth, Texas (KFWD) [see, e.g., Angevine et al. (2003) and Heaviside et al. (2015) for urban heat advection studies]. Furthermore, IGRA sites impacted by the coastal advection of the MBL, such as Corpus Christi, Texas (KCRP), Brownsville, Texas (KBRO), Slidell, Louisiana (KASD), and Lake Charles, Louisiana (KCWF), were also excluded [see, e.g., Lee and Pal (2017) and Pal and Lee (2019a) for coastal advection studies]. Last, we did not use measurements obtained in 2019 because much of the central Great Plains were impacted by the 2019 Mississippi and Missouri River valley flooding (Pal et al. 2020b).

We used 0000 UTC rawinsonde-derived profiles to determine z_i because we are interested in the front-relative z_i changes during the daytime (see section 3a for additional details). Also, the rawinsonde-based method to derive z_i used here is more

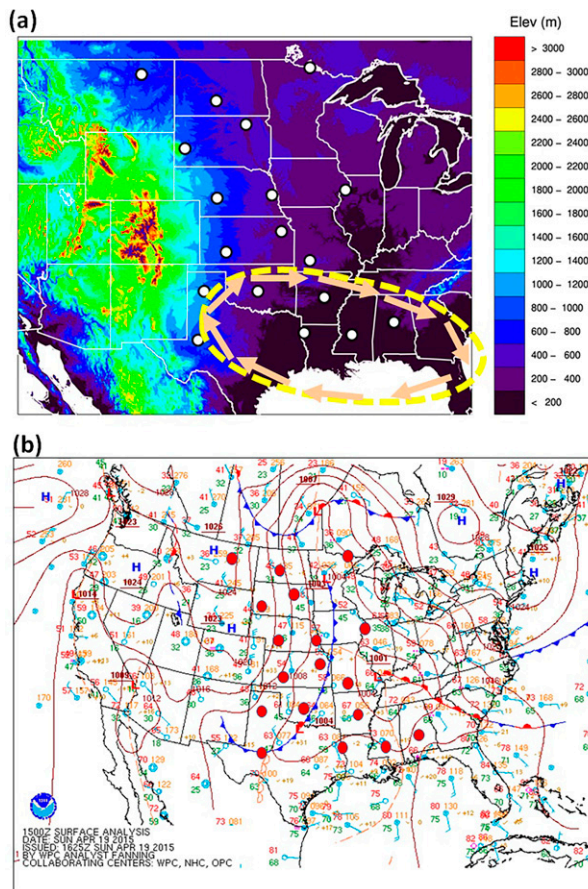


FIG. 1. (a) Locations of 18 NWS upper-air network sites (i.e., IGRA sites; white-filled circles) overlaid on a topographical map (site elevation; m MSL). The yellow-dashed region with arrows showing the horizontal wind direction marks a typical extension of the Bermuda high during summer months impacting regional-scale flow patterns over some portions of the experimental domain. (b) An example surface synoptic chart (1500 UTC 19 Apr 2015) used in the analyses for detecting frontal passages over the IGRA sites. Red filled circles mark the locations of the 18 sites relative to the cold-frontal boundary extending from central Minnesota to western Texas. The surface chart was obtained from NOAA's Weather Prediction Center.

appropriate for the daytime ABL than the nocturnal ABL (Lee and De Wekker 2016; Lee et al. 2018). We obtained the profiles of thermodynamic variables from the IGRA (Durre and Yin 2008) database (<https://www.ncdc.noaa.gov/data-access/weather-balloon/integrated-global-radiosonde-archive>) and synoptic surface maps from the NOAA Weather Prediction Center (<https://www.wpc.ncep.noaa.gov/archives/sfc/>).

3. Methods

a. Determination of ABL depth (z_i)

We determined z_i from the rawinsonde profiles using the bulk Richardson number Ri_b method outlined in Lee and De

Wekker (2016) and Lee and Pal (2020). In brief, we filtered the near-surface stable layer from the 0000 UTC IGRA sounding (i.e., via estimating the altitude where the virtual potential temperature gradient exceeded 0) and took z_i to be the first height at which Ri_b exceeded a critical value, which was set to 0.25 following previous work (e.g., Vogelesang and Holtlag 1996). The vertical resolution of the thermodynamic variables measured using the rawinsonde was 30–60 m depending on the ascent rate of the soundings (e.g., Durre and Yin 2008; Lee and Pal 2017). Since the early evening transition of the ABL often occurs before sunset and the rawinsonde launch time (i.e., 0000 UTC) and a nocturnal boundary layer has almost entirely developed (i.e., 1 h past sunset), the z_i -retrieval method used here mainly determines the altitude of the residual layer (RL) top. Based on Stull (1988), we have assumed that the daytime ABL top has become the top of the RL after sunset (see Fig. 1.7 in Stull 1988), and thus the method used here should provide an accurate estimation of the afternoon ABL prior to the evening transition. This method was previously used in several studies, including Seidel et al. (2010, 2012), Lee and De Wekker (2016), and Lee and Pal (2017). Recently, Strobach (2022) used a new method to determine both the depth and center of the RL based on the Ri_b gradient, which may be more appropriate for future work.

After determining z_i , we analyzed the water vapor mixing ratio q (g kg^{-1}) and potential temperature θ (K) profiles and estimated ABL- q (i.e., mean q within the ABL) and ABL- θ (i.e., mean θ within the ABL) by averaging q and θ samples across a thickness of 100 m centered at an altitude of $z_i/2$. We note that while determining ABL- q and ABL- θ we excluded q and θ values observed in the surface layer, stable boundary layer, and entrainment zone (EZ) around z_i , which often significantly varies in altitude (e.g., surface layer peak in q ; decreasing and increasing tendencies in q and θ , respectively, in the EZ). Nonetheless, based on previous work (e.g., Mahrt 1991; Kaimal and Finnigan 1994; Pal and Haefelin 2015), we found it appropriate to average a 100-m thickness across $z_i/2$ for determining ABL- q and ABL- θ .

b. Accumulation of surface charts for identifying fronts

We determined frontal passages using 3-hourly surface synoptic charts (i.e., eight surface maps per day) for the 5-yr period. Rather than downloading the individual synoptic charts manually, we used a Shell script function (i.e., wget.exe) to cumulatively import more than 7000 three-hourly surface charts for summer (June, July, and August) and winter (December, January, and February) each year for five years. The Shell script utilizes the unique URL address assigned to each surface chart and automatically downloads the respective image file for the user-defined time period (here, from 1 December 2013 to 31 December 2018). Note, the script used for this work can download any other file type from any source directory, provided the URL address is accessible. We made this Shell script available for users on GitHub (<https://github.com/nicholc/front-abl-classification>). Additionally, we provided the source code and a step-by-step guide for using the code in appendix E to improve the reproducibility of our results.

c. Classification of front-relative ABL regimes

Once the surface charts were available, they were treated with a newly developed framework to determine the front-relative location of each rawinsonde site during the 0000 UTC sounding. The framework we introduced primarily uses two concentric circles (200- and 400-km radii for inner and outer circles, respectively) around an individual site (e.g., Topeka, Kansas; Springfield, Missouri; and Norman, Oklahoma, as illustrated in Fig. 2). The values of radii to determine the front-relative location of the sites were chosen arbitrarily. In the context of this work, we referred to fronts located at or within the 200- and 400-km radii centered at each IGRA site as near- and moderate-distance frontal boundary types, respectively. The distance of the frontal boundary to the location of sounding (IGRA site) was determined using the radial distance from the IGRA site to the closest point of the front, as illustrated in Fig. 2a. Note that the overlays of 200- and 400-km-radius circles for each 0000 UTC surface chart were visualized rather than explicitly generated using a code. Future work will benefit from a more explicit treatment of this step (i.e., developing a code to perform the overlay).

After determining the distance of the soundings from the closest point of the front, the soundings were further divided into two major categories: prefrontal (i.e., warm sector) and postfrontal (i.e., cold sector) regimes. Here, prefrontal soundings occur prior to the frontal passage, and postfrontal soundings occur after the frontal passage. Consequently, our framework provided four unique classifications of the z_i measurements: 1) moderate prefrontal, 2) near prefrontal, 3) near postfrontal, and 4) moderate postfrontal.

To further illustrate the method, we refer back to Fig. 2a, which shows the 200- and 400-km-radius concentric circles we visualized over the 18 IGRA sites. Figures 2b–f display these overlays over 3 of the 18 sites (Topeka, Norman, and Springfield). As the front passes over each site, the color of the overlay was changed from blue to red depending on the location of the front. The red-shaded overlay indicates the classification that was assigned to the 0000 UTC measurement during the frontal passage. For instance, Fig. 2b indicates that the 0000 UTC sounding at Topeka was classified as near prefrontal due to the closest point of the front being located at or within the 200-km-radius circle and the sounding taking place prior to the frontal passage. The soundings at Norman and Springfield were classified as moderate prefrontal due to a similar reasoning. The bottom of Fig. 2a notes the classifications identified for the soundings that took place during this particular frontal passage. Note that this frontal passage took approximately 4–5 days to completely exit the region used to classify the soundings. This process was repeated for all 18 sites for two seasons spanning over the 5-yr period as illustrated in Fig. 3.

During this classification, we ensured that the frontal passages were treated in such a way so that front-relative contrasts in z_i , θ , and q were related to only a single front, meaning changes in pre- and postfrontal values were analyzed with respect to the same front. As such, a sounding cannot be both pre- and postfrontal at any point during a frontal passage.

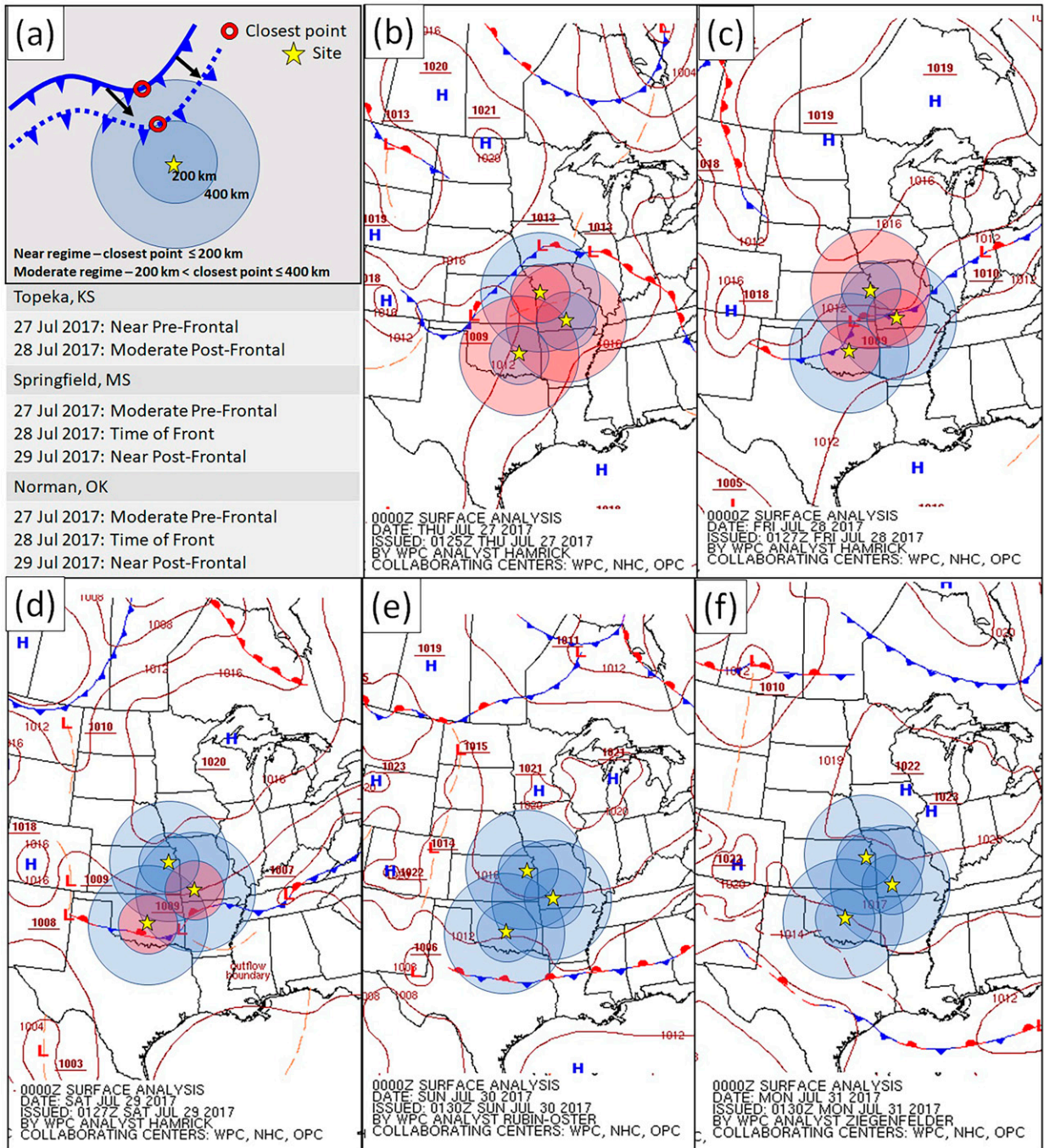


FIG. 2. (a) A schematic illustrating the determination of front-relative location of the IGRA site for both near- and moderate-distance prefrontal z_i sampling. The red circle and the yellow stars mark the closest point of intersection of frontal boundary and location of IGRA sites, respectively, and the solid and dashed blue lines with triangles mark the cold-frontal location for moderate- and near-distance frontal location, respectively. The radii for both near-distance (200 km) and moderate-distance (400 km) z_i sampling are also indicated. Also shown are the locations of three IGRA sites (yellow stars) overlaid on the synoptic maps (0000 UTC) along with the near- and moderate-distance locations (circles around the IGRA sites) illustrating the four z_i sampling regimes (near prefrontal, moderate prefrontal, near postfrontal, and moderate postfrontal) for soundings on (b) 27, (c) 28, (d) 29, (e) 30, and (f) 31 Jul 2017. Final front-relative z_i sampling dates for all three sites are also given in (a).

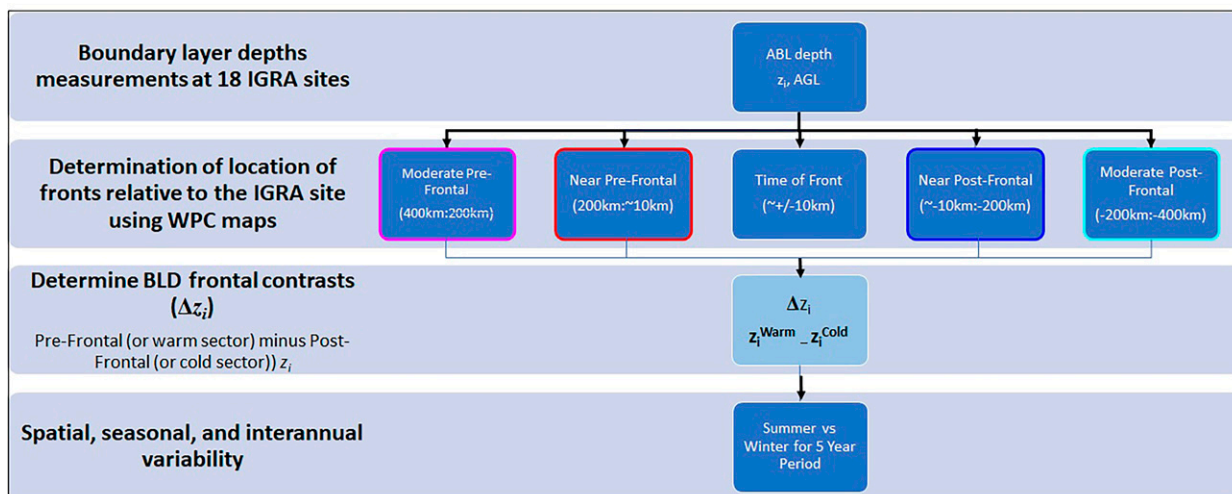


FIG. 3. Flowchart showing the steps involved in the data-analysis method to determine frontal contrasts in z_i (i.e., Δz_i) over the 18 sites for summer and winter during the measurement period 2014–18. The color of the boxes for ABL regimes identified as moderate-distance prefrontal, near prefrontal, near postfrontal, and moderate-distance postfrontal was kept magenta, red, blue, and cyan, respectively. Similar color codes were used for Figs. 6 and 9, below.

Thus, after a prefrontal sounding is recorded, we must wait a minimum of 24 h for the front to pass over the IGRA site and the next 0000 UTC sounding to be considered for the z_i retrieval and subsequent analyses.

Additionally, since the thermodynamic conditions and factors that impact frontogenesis differ with each front, yielding different ABL dynamical regimes (e.g., Hoskins and Bretherton 1972; Doswell and Haugland 2007), frontal passages that occur in quick succession (i.e., two frontal boundaries located within the 400-km circle at 0000 UTC) to one another may sometimes prevent an appropriate analysis of pre- and postfrontal ABL regimes. These instances were avoided in this work. As a result, many northern sites such as Glasgow, Montana, often observed fewer front-relative z_i samples than did southern sites as shown in Fig. B1 in appendix B). We attribute the quick succession of cold-frontal passages in the northern part of the United States (e.g., northern Great Plains, northeastern sector) to stronger frontal passages that occur more frequently relative to the southern part (e.g., southern Great Plains and southeastern United States), which is a typical characteristic of midlatitude cyclones over the United States. Overall, Fig B1 shows the number of instances when front-relative z_i measurements were available for all four classifications over all sites in different years.

The number of front-relative z_i cases for any site depended on a variety of factors, including 1) availability of rawinsonde profiles at the site, 2) successful retrieval of z_i from rawinsondes at 0000 UTC, 3) more than 400-km horizontal distance between the location of the frontal boundary at 0000 UTC and the IGRA site, and 4) the occurrence of multiple fronts within the 400-km overlay. Since this is the first time a method was introduced for investigating z_i frontal contrasts based on surface charts and regular rawinsondes, extreme caution was taken so that only clearly defined cold-frontal boundaries were selected. This conservative selection method might have

ignored many perfectly suitable frontal passages. Identifying appropriate soundings to use for analysis might be challenging but not impossible. Nevertheless, the low number of samples and associated data gaps in the z_i observations for both pre- and postfrontal regimes remain a potential limitation of this work.

In summary, the method to investigate the front-relative z_i variability consists of three major steps (Fig. 3): 1) identifying the sites and location of frontal passages around 0000 UTC (i.e., the start time of the launch of the rawinsonde measurement), 2) segregating the observed z_i using two flags: prefrontal (warm) and postfrontal (cold), depending on the location of the frontal boundary, and 3) estimating the front-relative z_i contrasts (i.e., $\Delta z_i = z_i^{\text{Warm}} - z_i^{\text{Cold}}$) across the two regimes.

4. Results and discussion

a. Variability of z_i in pre- and postfrontal sectors in summer and winter

A comprehensive overview on the z_i variability within the four front-relative ABL regimes [moderate-distance-prefrontal and near-prefrontal regimes (i.e., warm-sector ABL regimes) vs moderate-distance-postfrontal and near-postfrontal regimes (i.e., cold-sector ABL regimes)] over the 18 sites during summer and winter for the period 2014–18 is shown in Figs. 4 and 5, respectively. In each heat map, the pixels represent the median z_i observed during the respective season over each site. Additionally, box-and-whisker plots of z_i variability for each front-relative ABL regime observed at the 18 IGRA sites for the 5-yr period during summer and winter are presented in appendix C (Figs. C1 and C2), yielding additional details on the site-specific z_i features relative to the different frontal boundaries associated with the variability. Since this work does not aim to investigate the z_i seasonal variability already

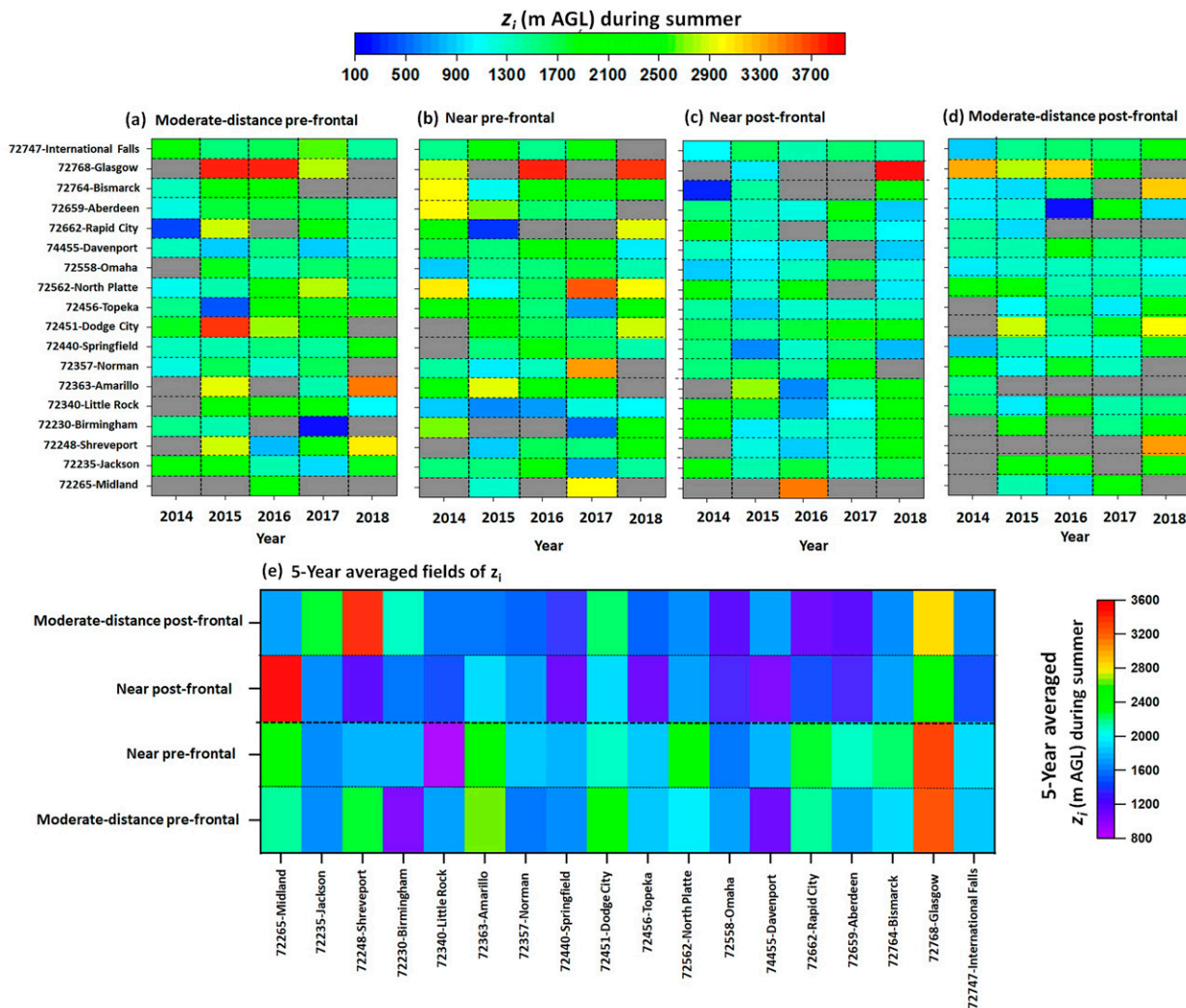


FIG. 4. Heat-map view of summertime z_i over the 18 IGRA sites during sampling times for the regimes identified as (a) moderate-distance prefrontal, (b) near prefrontal, (c) near postfrontal, and (d) moderate-distance postfrontal, showing the impact of frontal passages on z_i . Also shown is (e) a consolidated view of all four panels obtained by averaging over the 5-yr period, yielding overall prefrontal vs postfrontal z_i variability for both moderate- and near-distance samplings. The color-bar scale limit in (e) is different than in the other panels to show the overall cross-frontal z_i variability. Prefrontal and postfrontal refer to warm and cold sectors, respectively, and have been used interchangeably. The sites are arranged from south to north along the y axis by their latitudes, and (a)–(d) are arranged from west to east (moderate prefrontal, near prefrontal, near postfrontal, and moderate postfrontal) such that cold-frontal passes from west (or northwest) to east (southeast). Similar configurations of both x axis and y axis are maintained in all other figures. Gray pixels denote gaps in pre- or postfrontal sampling of z_i . In (e), the sites are arranged from south to north along the x axis by their latitudes, and the solid dotted grid line separates the prefrontal (warm) and postfrontal sectors in the bottom and top two pixels along the y axis, respectively.

discussed in numerous studies in the past (e.g., Yi et al. 2001; Seidel et al. 2010, 2012; Zhang et al. 2013; Pal and Haefelin 2015), we used different color-bar scale limits in Fig. 4 than in Fig. 5. Nevertheless, our results show that z_i over all the sites in winter were shallower than in the summer, although this should not be considered as a major finding in the context of this work.

Both Figs. 4 and 5 display systematic observations of ABL processes occurring in both the warm and cold sectors and show more instances with deeper z_i in the warm sector than in the cold sector (see more warm colors in prefrontal samples than in postfrontal samples) over most of the sites with few

exceptions. To further illustrate this point, a consolidated view of all four panels (Figs. 4a–d and 5a–d) is presented via averaging over the 5-yr period, which further confirms deeper z_i in the prefrontal sector than in the postfrontal in summer and winter for both moderate- and near-distance samplings (Figs. 4e and 5e).

For summer for the z_i differences observed between Topeka and Dodge City, Kansas (500 and 3800 m AGL, respectively), we note that a one-to-one comparison for z_i in the region is not straightforward, given they may not be related to the same frontal system. We also note that Dodge City (791 m MSL) is

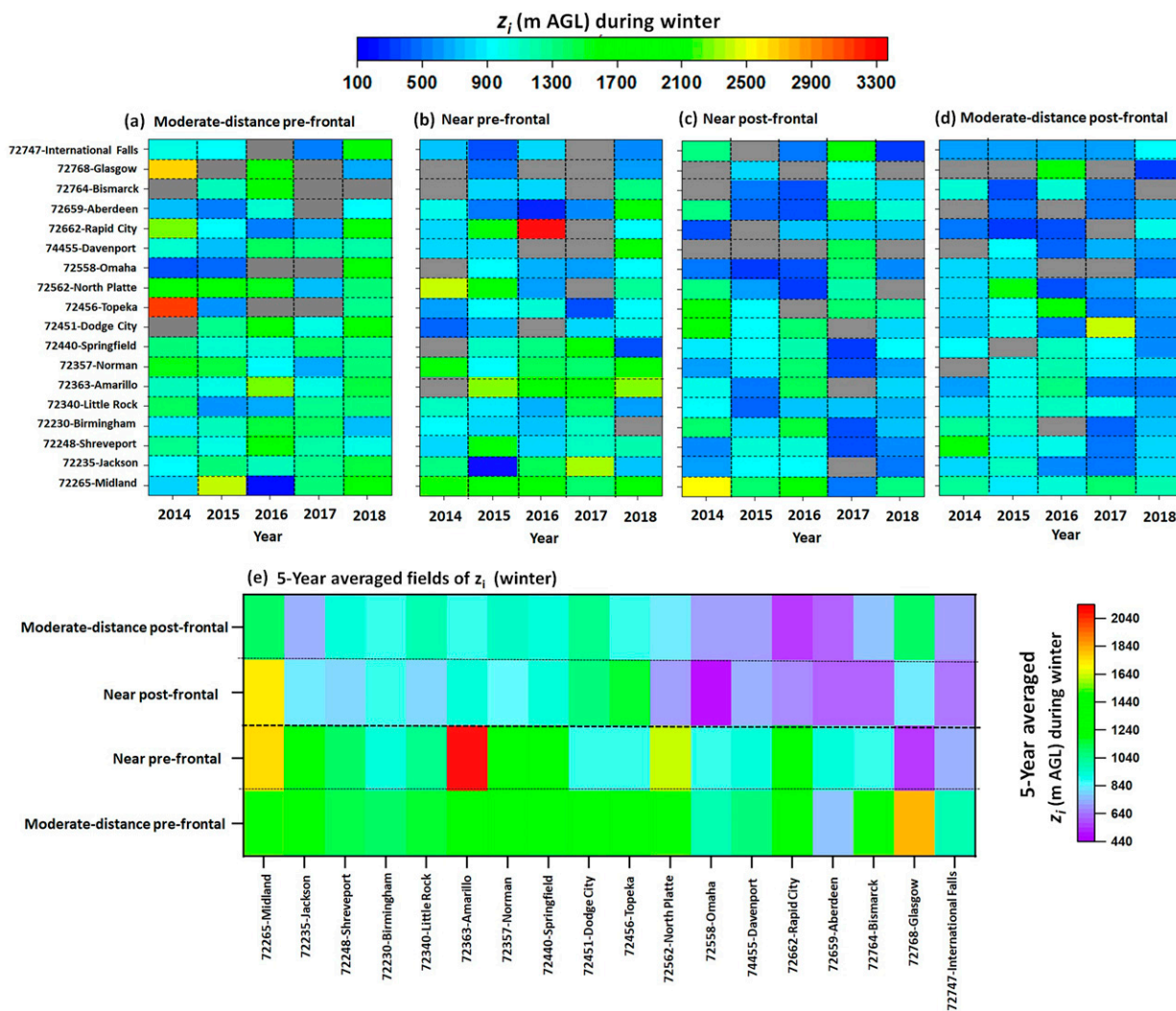


FIG. 5. As in Fig. 4, but for z_i during winter over all the sites. The color-bar scale limits are kept different than in Fig. 4 so that front-relative z_i changes Δz_i during winter across the sites are visible and because z_i seasonal variability (i.e., summer vs winter differences) is not intended here.

located closer to the Rocky Mountains than Topeka (268 m MSL), and thus some impact of advection on the z_i measurements by the adjacent complex terrain during the frontal passages at Dodge City cannot be ruled out (e.g., Stensrud 1993; Pal and Lee 2019b).

As mentioned, we typically observed deeper z_i in the pre-frontal sector than in the postfrontal sector. However, for two sites in winter (i.e., Topeka in 2014 and Rapid City, South Dakota, in 2016), contrasting results were found (i.e., deeper z_i in the postfrontal sector), likely related to the impact of advection from the mountainous regions, which has been discussed in previous studies (e.g., Stensrud 1993; Pal and Lee 2019b). In general, complex terrain often significantly impact the representation of the ABL, even in the absence of frontal boundaries (e.g., Pal et al. 2016; Rotach et al. 2022). Hence, we assert that future work may focus on the combined impact of frontal passages and orographic influences on z_i variability.

Next, we compared the front-relative z_i features at different sites in different years. We note that it remains challenging to perform a one-to-one comparison between neighboring sites because the analyzed z_i are most likely from different frontal systems. Thus, the results showing the 5-yr-averaged z_i features within each front-relative ABL regime suggest some variability that could be attributed to the impact of both different types of frontal systems and the interannual variability (Fig. 6; see standard deviation values). We noted such variability was more prominent in the warm sector (Figs. 6a,b) than in the cold sector (Figs. 6c,d), except at a few northern sites. The σ_{z_i} values (in the box-and-whisker plots) most likely also show more of the z_i variability from different frontal systems than it does interannual variability. Nevertheless, these results illustrate how ABL features (z_i in this instance) differ

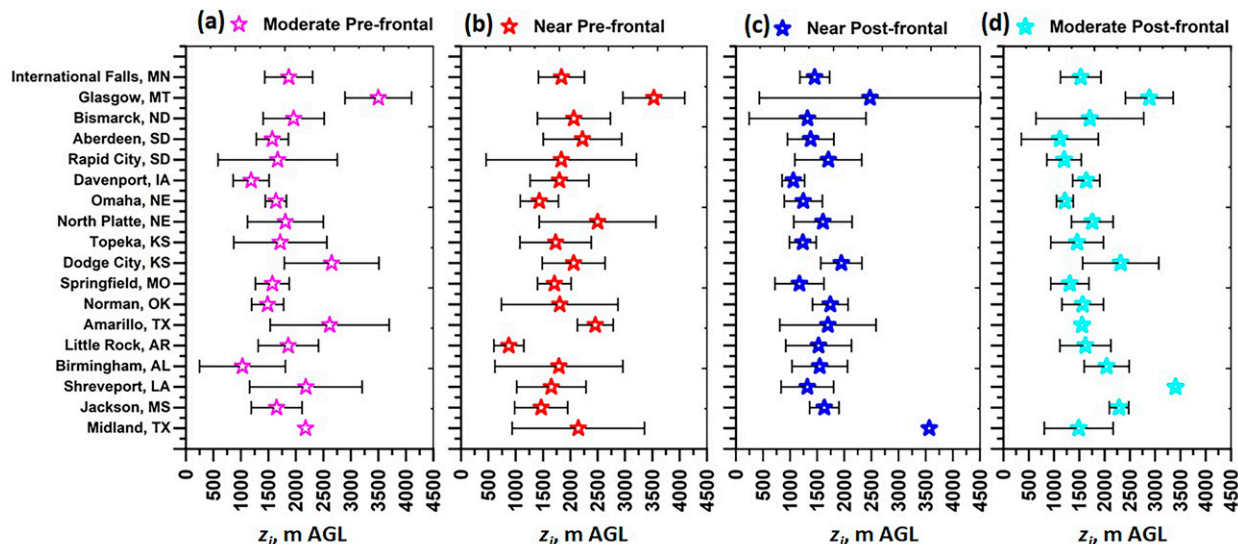


FIG. 6. An overview of the z_i variability averaged over a 5-yr period at 18 IGRA sites for four front-relative ABL regimes [(a) moderate prefrontal, (b) near prefrontal, (c) near postfrontal, and (d) moderate postfrontal] at all sites. Stars mark the means, and horizontal bars represent ± 1 std dev of observed z_i at each site. Sites are arranged from south to north (see the y axis).

between frontal sectors. In general, these results (Figs. 4–6) showcase the impact of frontal passages on z_i variability during summer and winter. Future work on the interannual z_i variability will provide more insight on this topic.

For summer, the site-to-site z_i variability in the warm sector (i.e., z_i standard deviations σ_{z_i} of 722 and 797 m for moderate-distance and near-distance prefrontal ABL regimes, respectively; see the 5-yr-averaged column in Table 1) was found to be larger than in the cold sector (i.e., σ_{z_i} of 601 and 658 m). Similarly, for winter, we found that the z_i variability among the sites in the warm sector was larger (i.e., σ_{z_i} of 502 and 622 m for moderate-distance and near-distance prefrontal ABL regimes, respectively) than the cold sector (i.e., σ_{z_i} of 445 and 387 m; Table 1). We note the site-to-site variability (i.e., σ_{z_i}) also varies among the years for both warm (prefrontal) and cold (postfrontal) sectors for both summer and winter (see Table 1). While comparing z_i variability between warm and cold sectors, results revealed that the warm-sector z_i variability was 31% and 30% higher than the cold-sector z_i variability, in

summer and winter, respectively. Relatively lower z_i variability in postfrontal than the prefrontal regime suggests either that the air mass properties have a larger impact on z_i growth for the postfrontal air mass or that this air mass is less variable through the year. However, further research is needed to confirm the relationship between air mass types and z_i variability. In general, these findings suggest a more vigorous and dynamically unstable ABL regime in the vicinity of the frontal boundary and a more diverse impact of advection in the warm-sector flows than in the cold sector.

b. Discussion of z_i contrasts across frontal boundaries in summer and winter

Based on the method discussed in section 3, we obtained front-relative z_i contrasts for both moderate- and near-distance frontal boundary locations across the warm (i.e., prefrontal) and cold (i.e., postfrontal) sectors for both seasons; corresponding results are shown via box-and-whisker plots (Fig. 7), where N refers to the number of samples for each site. These

TABLE 1. An overview of the site-to-site z_i variability (i.e., σ_{z_i} ; m) in the prefrontal (warm) and postfrontal (cold) sectors for both moderate-distance and near-distance samples in all five years and also for 5-yr-averaged fields.

Frontal regimes	2014	2015	2016	2017	2018	Averaged over 5 yr
Summer						
Moderate prefrontal	456	945	729	713	767	722
Near prefrontal	770	738	686	932	858	797
Near postfrontal	597	473	711	429	797	601
Moderate postfrontal	726	630	741	412	781	658
Winter						
Moderate prefrontal	735	483	605	320	367	502
Near prefrontal	606	592	773	603	534	622
Near postfrontal	594	316	511	511	294	445
Moderate postfrontal	342	332	507	533	219	387

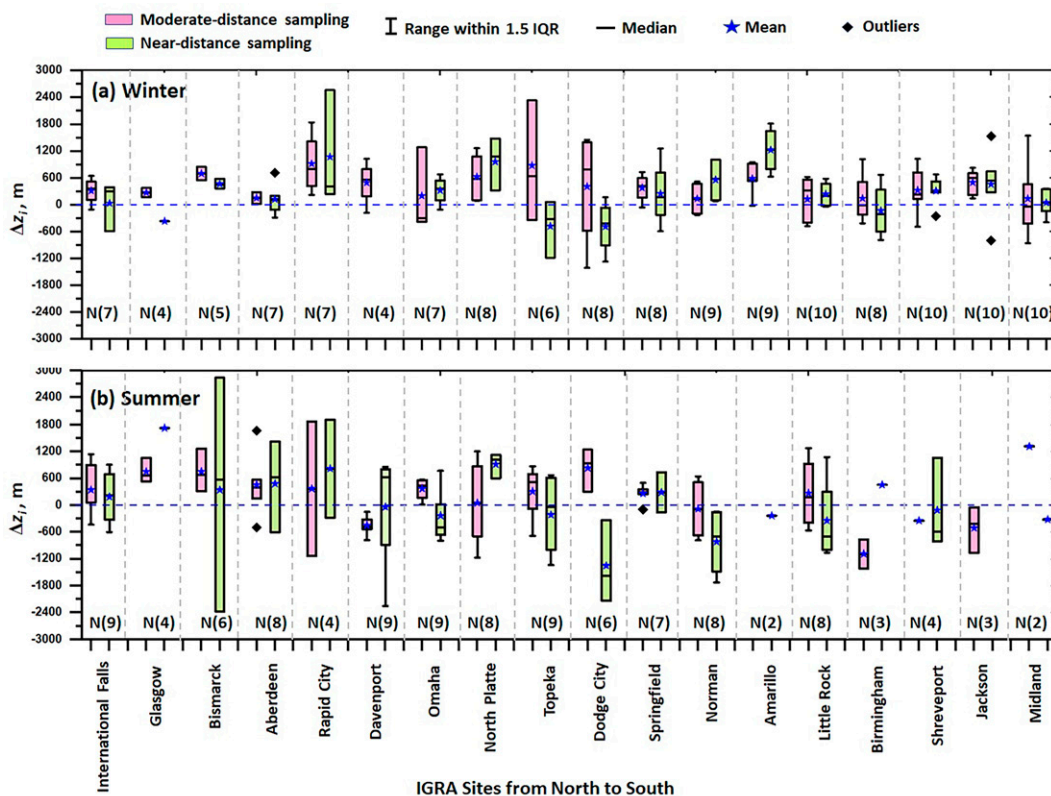


FIG. 7. Box-and-whisker plots of Δz_i (i.e., $z_i^{\text{Warm}} - z_i^{\text{Cold}}$) across frontal boundary (magenta boxes: moderate-distance sampling; light-green boxes: near-distance sampling) over the 18 IGRA sites illustrating the impact of frontal passages on z_i during (a) winter and (b) summer. The thick horizontal line and star mark the median and mean values of the distributions, respectively. The boxes correspond to 25%–75% percentiles of the distributions, the whiskers correspond to the $1.5 \times$ interquartile range (IQR), and the black diamonds indicate the outliers. The sites are arranged from north to south along the x axis. The horizontally aligned blue dashed line on each panel marks the zero line (i.e., no frontal contrasts in z_i , or $\Delta z_i = 0$), and N values denote the number of total samples for each site for different front-relative z_i estimations.

analyses show distributions of Δz_i across the different ABL regimes with respect to the relative location of the IGRA site to the frontal boundaries.

To the best of the authors' knowledge, it remains instructive to discuss Δz_i variability for both ABL regimes over the 18 sites and their features in summer and winter. For winter, the results suggest that 1) mean Δz_i for both ABL regimes over all the sites were primarily positive, illustrating deeper z_i over the warm sector than the cold sector, except two instances over Topeka and Dodge City for near-distance prefrontal ABL sampling, 2) mean Δz_i over all the sites range from 100 to 900 m for moderate-distance and from 100 to 1200 m for near-distance ABL sampling, and 3) the largest spread in Δz_i was observed over the central Great Plains (e.g., Rapid City; Davenport, Iowa; North Platte, Nebraska; Topeka; and Dodge City).

In general, results on the z_i contrasts Δz_i across the frontal boundary in summer and winter reveal substantial site-to-site variability in the near-distance frontal sampling than in the moderate-distance sampling. For instance, we found Δz_i standard deviations to be 673 and 629 m for near- and moderate-distance

frontal sampling, respectively, in the winter. However, unlike in summer, z_i contrasts in winter were more prominent in the southern sites than in the northern sites. For instance, over the sites located in the southern Great Plains and southeastern United States (e.g., Amarillo, Texas; Little Rock, Arkansas; Birmingham, Alabama; Shreveport, Louisiana; Jackson, Mississippi; and Midland, Texas), mean Δz_i varied from -1200 to 300 m without any apparent pattern (see Fig. 7). This could be attributed to the stronger and larger southern extension of cold-frontal passages over the southern plains in winter than in summer due to the limited extension of the Bermuda high over the region in summer, which often impedes the progression of frontal passages toward the southern part of the United States (Fig. 1a) (e.g., Wang et al. 2016; Davis et al. 1997). DiMego et al. (1976) reported that the frequency and strength of the cold fronts into the southern region of the United States are mainly related to the magnitude and amplitude of the midlatitude circulation and found an increasing frequency of these passages from autumn to winter and a decreasing frequency from spring to summer.

Additionally, among the four ABL regimes, the z_i frontal contrasts (i.e., Δz_i) were found to be much larger for the near-

prefrontal regime versus the near-postfrontal regime (Fig. 7), and the frontal contrasts were found to be more prominent in winter than in summer. The latter can be attributed most likely to the relatively stronger frontal passages in winter than in summer, as suggested by relatively larger frontal contrasts in $ABL-\theta$ [see larger color-bar ranges in theta of 40 K (winter) and 18 K (summer) in Figs. D4e and D3e, respectively, in appendix D].

For summer, we found that, unlike in winter, Δz_i did not have a clear pattern over all the sites; instead, we found that most of the observed Δz_i were positive over the northern sites and negative over the southern sites (Fig. 7b). For a majority of the cases over the IGRA sites located in the northern Great Plains (International Falls, Minnesota; Glasgow; Bismarck, North Dakota; Aberdeen, South Dakota; Rapid City; Davenport; and Omaha, Nebraska), we found the mean Δz_i varied from 100 to 900 m. Also, in general, previous studies on frontogenesis showed that the frontal strength in summer over land is much weaker than in autumn and winter (e.g., Davis et al. 1997; Li et al. 2011).

As a disclaimer, we note there exists some discrepancies in the total number of points N as they were not evenly distributed between the moderate and near sampling distance and pre- and postfrontal samples (e.g., z_i results presented for Midland in Fig. 7b). More high-resolution and continuous information on the z_i variability across frontal boundaries would be helpful to provide more robust and statistically significant results in future. We also note the small number of points for each site might also be associated with different stages of frontogenesis. For this reason, the mechanisms that enhance or reduce frontogenesis will lead to dynamical changes that are reflected on either side of the front, which will additionally manifest in the slantwise structure of the front and thereby impact the cross-frontal z_i variability (i.e., Δz_i). Additionally, the “near frontal” position, for example, is not a constant distance from the site. The sampling method allows for the frontal boundary to be located anywhere between the site and the nearest 200 km radial distance from the site when the 0000 UTC sounding is launched. Since the width of the front is on that order, it was not feasible to consider the impact of the different stages of pre- and postfrontal regimes on z_i variability. Within future work, resolving these issues for the relevant z_i variability would allow for a more comprehensive evaluation on the impact of frontal passages on z_i over land. Despite the differences among Δz_i over different sites and the limitation of the number of samples for different sites, a clear impact of frontal passages on z_i variability can be discerned.

A frequency distribution analysis of the observed Δz_i for both moderate- and near-distance ABL sampling revealed that the number of Δz_i samples was larger in winter (136) than in summer (108). This was mainly due to the lower number of frontal passages in summer than in winter, in particular for the southern sites as illustrated before. Overall, the results suggest that frontal passages trigger substantial site-to-site variability in the front-relative z_i contrasts (Δz_i) in both summer and winter, which we attribute to the combined impact of

changes in land surface forcing and z_i advection pertaining to the airmass exchange.

Because of a lack of collocated rawinsonde profiles and frontal passage over the IGRA sites (i.e., 0000 UTC sounding and cold front moving over the site at 0000 UTC), it was not possible to systematically compare z_i variability precisely at the time of frontal passage over the site with the z_i observed on the preceding and succeeding days of the frontal passage. Nevertheless, we demonstrated that once the quasi-regular z_i variability is segregated according to airmass sectors (i.e., relative to passages of midlatitude cyclones), one may obtain important information on the impact of frontal passages on z_i over land. Although frontal strength varies as a function of time, we assumed in this study that the larger environmental conditions remained steady.

We also provided box-and-whisker plots of contrasts in mean q within the ABL across the frontal boundaries (i.e., Δq_{ABL}) for all the z_i samples over all the sites for both seasons (Fig. 8). We noted an ABL- q contrast (i.e., Δq_{ABL}) in both summer (4–8 g kg⁻¹) and winter (6–8 g kg⁻¹), with higher (~45%–55% depending on the sites) ABL- q in the warm sector than the cold sector for both moderate- and near-distance frontal sampling, though with variable Δq_{ABL} strengths among the sites. This feature for southern sites was more prominent and persistent in winter than in summer. Also, southern sites experienced much stronger frontal contrasts in ABL- q (i.e., higher Δq_{ABL}) than the northern sites because of closer proximity and enhanced moisture transport from the Gulf of Mexico in the warm sector (see Figs. D1 and D2 in appendix D). Typically, during the Northern Hemisphere summer over the United States, the southerly flow brings consistently deep, moisture-laden maritime air into the southeast United States (e.g., Davis et al. 1997), presumably affecting the measurements at the IGRA sites in Louisiana, Mississippi, and Alabama.

Similar box-and-whisker plots for mean potential temperature within the ABL (i.e., ABL- θ) for all four ABL regimes are reported in Figs. D3 and D4 in appendix D, which also show the front-relative ABL- θ patterns (i.e., warmer ABL- θ in the prefrontal than in the postfrontal regimes). This fact becomes evident if one notes the ABL- θ ranges in winter (48 K varying from 258 to 318 K) was ~85% larger than in summer (26 K varying from 292 to 318 K), confirming the stronger frontal strengths in winter than in summer; a typical feature of frontogenesis over the continental United States (Shafer and Steenburgh 2008; Pal et al. 2020a). However, a direct comparison between front-relative differences in ABL- θ and surface temperature (typically referred to as frontal strength) in the context of this study is not straightforward (e.g., Sanders and Doswell 1995; Lee et al. 2012) because frontal strength obtained using surface temperature differences are significantly influenced by the diurnal cycle of temperature, which also changes spatially and seasonally.

Additionally, we do not attribute contrasts in ABL- θ to act as a cause or driver of the front-relative z_i changes. Instead, the aim of studying ABL- θ contrasts was to document the thermodynamic properties related to the pre- and postfrontal ABL air masses in the summer and winter. Future investigations will be helpful in this regard to determine the relationship

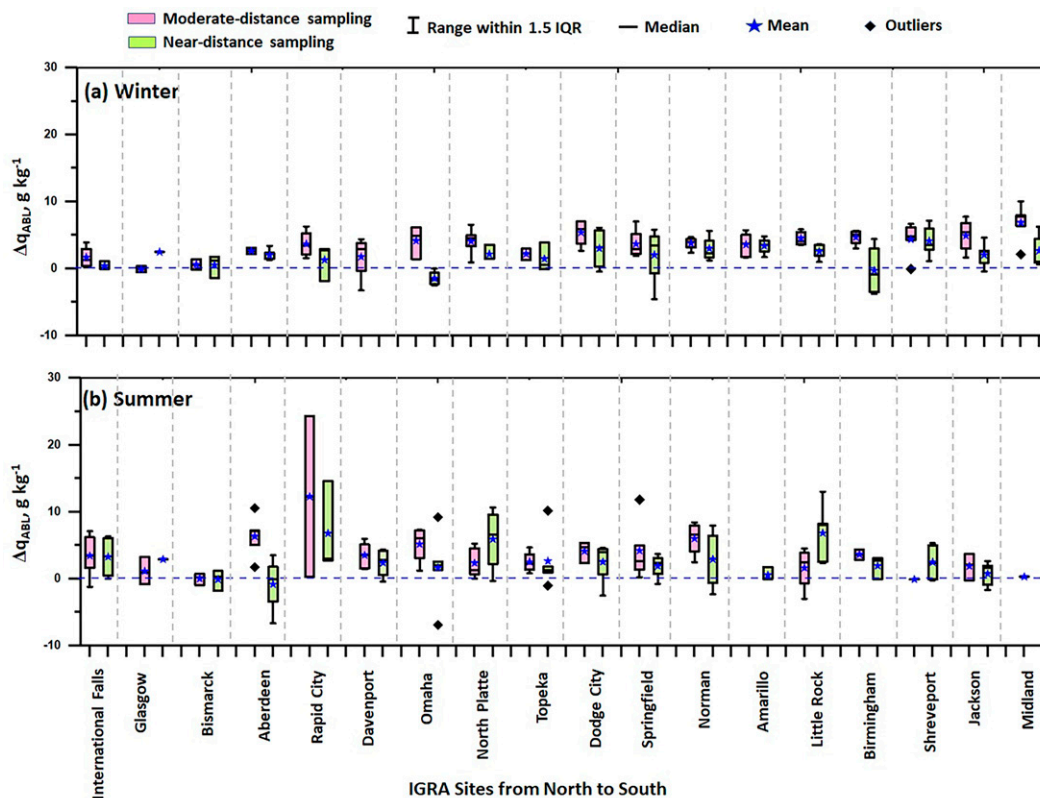


FIG. 8. As in Fig. 7, but for front-relative contrasts in ABL- q (i.e., Δq_{ABL}) over the 18 sites in (a) winter and (b) summer for the entire measurement period.

among Δz_i , front-relative differences in ABL- θ , and surface temperature.

The results presented for the Eulerian front-relative variability in ABL- q strongly support the signatures of Δq_{ABL} in a frontal environment over land, yielding lower ABL- q in the cold sector than the warm sector. Additionally, our approach represents overall what is typically observed in transient extratropical cyclones and their equatorward trailing cold fronts due to synoptic-scale descent of FT air in the cold sector (e.g., Carlson 1980; Browning 1997; Wernli 1997). Thus, the results presented set forth a potential pathway for documenting frontal signatures in z_i variability over land. Comparing the two panels of Fig. 8, we see that the front-relative Δq_{ABL} is higher in summer than in winter as expected for the Northern Hemisphere seasons. The influence of frontal passages on ABL- q over several continental sites for both seasons has not been addressed systematically thus far.

c. An integrated view on the z_i contrasts across frontal boundaries

Little attention has been paid to cross-frontal z_i features (i.e., Δz_i) over land, and thus it is not easy to make any direct comparison with past studies on this topic. The only exception to this is Sinclair et al. (2012), who reported positive Δz_i , though for a shear-dominated nocturnal ABL. Nevertheless, our results suggest that to resolve the major factors attributed

to the z_i variability over land on different time scales (diurnal, synoptic, and seasonal), one must consider the impact of advection of two air masses associated with frontal passages. Most of the climatological studies focusing on z_i variability on different time scales have mainly concentrated on the air-mass-independent z_i scenarios (e.g., Yi et al. 2001; Seidel et al. 2010, 2012; Zhang et al. 2013; Pal and Haeffelin 2015; Lee and Pal 2017). Thus, our results on the z_i contrasts across frontal boundaries in two seasons over land across a broad region help one argue that frontal passages should be acknowledged.

For brevity, to quantify and understand how the ABL moisture regimes occur during frontal passages and to establish an integrated overview of the z_i variability across frontal boundaries in both seasons, we averaged all the observed ABL- q and z_i over all the IGRA sites as shown via box-and-whisker plots (Fig. 9). Results reveal that z_i was deeper in the warm sector than in the cold sector during both summer and winter. Additionally, both Δq_{ABL} and $\Delta \theta_{\text{ABL}}$ were positive in both seasons during the frontal passages, though with significant site-to-site variability (Figs. D1–D4). When averaged across all the samples, we still observed a similar tendency in Δq_{ABL} during both summer and winter as was noted for individual sites, though with varying magnitudes. However, for summer, the near-distance pre- and postfrontal sampling did show a general reduction in z_i from the warm to the cold sector, but the moderate-distance ABL sampling did not indicate any significant change in z_i from the warm to the cold sector.

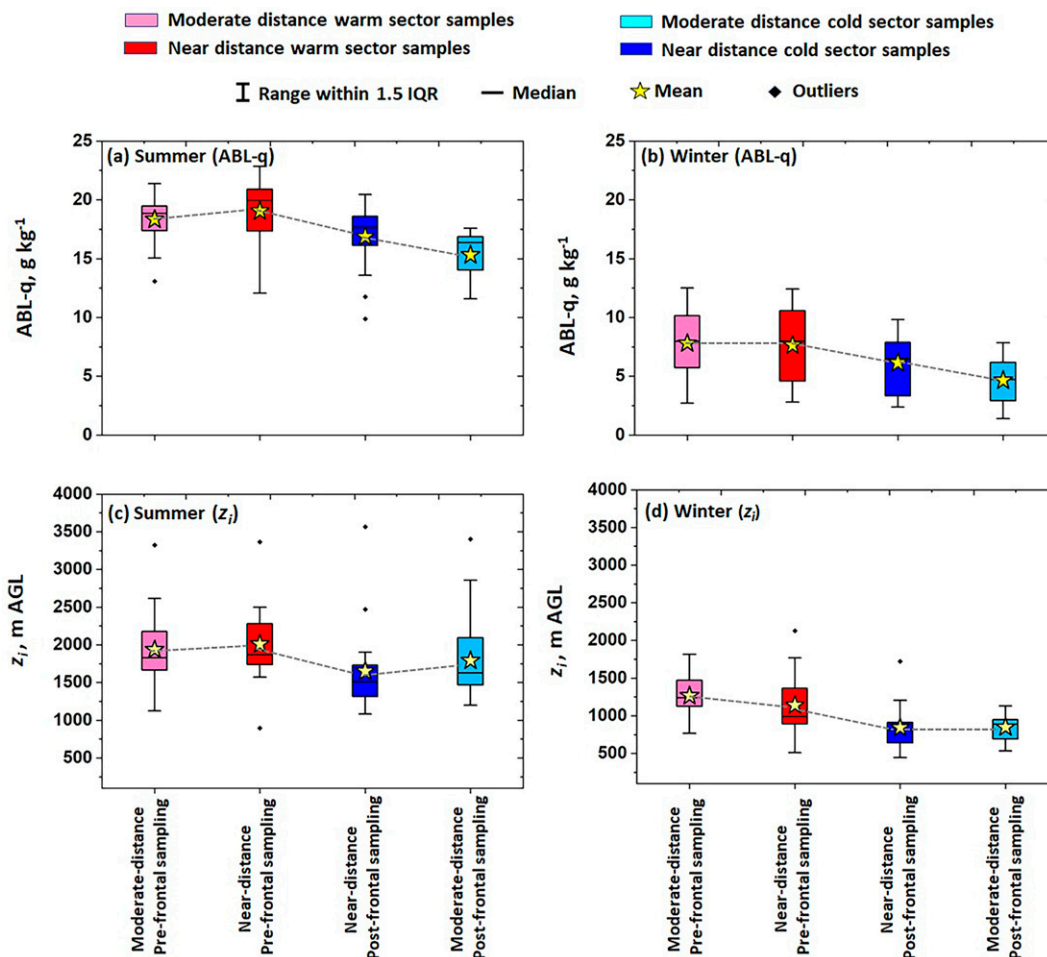


FIG. 9. Box-and-whisker plots of $ABL-q$ over the 18 sites during (a) summer and (b) winter illustrating overall frontal signatures in warm (i.e., prefrontal sampling) vs cold (i.e., postfrontal sampling) sectors. Also similarly analyzed is overall z_i variability across the frontal boundary in (c) summer and (d) winter. The symbols and other parameters appearing in the box-and-whisker plots are identical to symbols presented in Fig. 7, although yellow stars represent the means.

For the summer cases, while comparing the median values of both parameters (Fig. 9), we found Δq_{ABL} and Δz_i for moderate-distance ABL sampling to be 2.57 g kg^{-1} and 205 m, respectively, and found Δq_{ABL} and Δz_i for near-distance ABL sampling to be 2.49 g kg^{-1} and 363 m, respectively. A similar analysis for the winter cases revealed medians of Δq_{ABL} and Δz_i for moderate-distance ABL sampling to be 3.26 g kg^{-1} and 331 m, respectively, and for near-distance ABL sampling to be 1.68 g kg^{-1} and 196 m, respectively. From these analyses, a front-relative Δq_{ABL} of 1 g kg^{-1} would yield at least 100 m of Δz_i across the frontal boundary in both summer and winter. We also note that the results revealed interesting findings on the relationship between Δq_{ABL} and Δz_i , and there exist many opportunities for future investigations on this topic.

5. Summary and outlook

In this study we reported one of the dynamic processes (i.e., frontal passages) that affect the thermodynamics of the

ABL air mass over the land surface using 5-yr measurements of rawinsonde-derived daytime ABL depths (z_i) over 18 sites in the central and southeastern United States. We conducted this work by analyzing contrasts in z_i and mean boundary layer moisture mixing ratio (i.e., $ABL-q$) relative to the location of frontal boundaries (i.e., Δz_i and Δq_{ABL}) during summer and winter and explained the Eulerian front-relative variability in z_i and $ABL-q$ under two scenarios related to the locations of frontal boundaries (i.e., z_i in warm vs cold sectors). We also investigated Δz_i and explored z_i spatiotemporal variability as a function of weather patterns that allowed for the investigation of the impact of mesoscale processes on the ABL in association with cold-frontal passages trailing from transient cyclones in the midlatitudes.

Overall, based on the cases investigated using the front-relative z_i classifications introduced for two seasons, we found differences between z_i , yielding deeper z_i in the warm sectors than the cold sectors. For instance, during the summer, the warm-sector median z_i (1830 and 1870 m AGL for moderate- and

TABLE A1. List of the 18 NWS upper-air network sites with their IGRA site identifier (ID), International Civil Aviation Organization (ICAO) airport code (beginning with K), geographic location, and elevation.

IGRA site ID	Sites (U.S. state); airport code	Lat (°N)	Lon (°W)	Elev (m MSL)
72747	International Falls (MN); KINL	48.57	93.38	359
72768	Glasgow (MT); KGGW	48.21	106.63	694
72764	Bismarck (ND); KBIS	46.77	100.75	505
72659	Aberdeen (SD); KABR	45.45	98.41	397
72662	Rapid City (SD); KRAP	44.07	103.21	1027
74455	Davenport (IA); KDVN	41.62	90.58	229
72558	Omaha (NE); KMLE	41.32	96.37	350
72562	North Platte (NE); KLBF	41.13	100.68	847
72456	Topeka (KS); KTOP	39.07	95.62	268
72451	Dodge City (KS); KDDC	37.77	99.97	791
72440	Springfield (MO); KSGF	37.23	93.38	384
72357	Norman (OK); KOUN	35.23	97.47	358
72363	Amarillo (TX); KTDW	35.23	101.7	1094
72340	Little Rock (AR); KLIT	34.83	92.25	172
72230	Birmingham (AL); KBHM	33.17	86.77	178
72248	Shreveport (LA); KSHV	32.45	93.83	79
72235	Jackson (MS); KHKS	32.32	90.08	91
72265	Midland (TX); KMAF	31.95	102.18	873

near-distance sampling, respectively) were found to be 13% and 25% deeper in their respective sampling distances than the cold-sector median z_i (1628 and 1504 m AGL for moderate- and near-distance sampling, respectively). For winter, a similar trend was found; the warm-sector median z_i (1241 and 992 m AGL for moderate- and near-distance sampling, respectively) were 39% and 23% deeper in their respective sampling distances than the cold-sector median z_i (894 and 812 m AGL for moderate- and near-distance sampling, respectively). Thus, these results (note the percent values in Δz_i) confirm that there exist more prominent front-relative z_i contrasts in winter than

in summer. As was observed for Δz_i variability across the frontal boundary in winter, the average Δz_i also had a similar pattern (i.e., positive Δz_i yielded a general decrease in z_i from warm to the cold sector). Results revealed that a front-relative Δq_{ABL} of 1 g kg^{-1} would yield at least 100 m of Δz_i across the frontal boundary in summer and winter.

In addition to the previous research on this topic (i.e., ABL processes in coastal regions and areas of complex terrain illustrated in Pal and Lee 2019a,b), the results reported here provide another example in which advection plays an important role modulating z_i via air mass exchange. Specifically, we

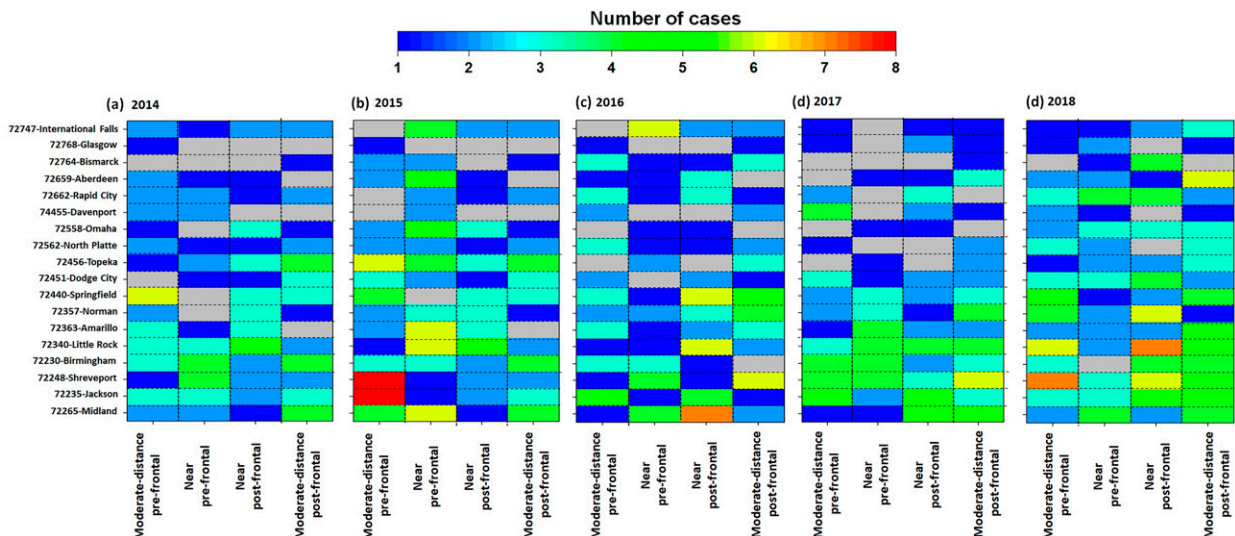


FIG. B1. An overview of the number of instances when front-relative z_i measurements were available over the 18 IGRA sites during the period 2014–18 for the four regimes (i.e., near prefrontal, moderate prefrontal, near postfrontal, and moderate postfrontal). The cold-frontal passages during which z_i measurements were available and the frontal boundaries were within the 400-km distance were only considered here, as discussed in section 2. Gray pixels mark gaps in pre- or postfrontal sampling of z_i over the sites.

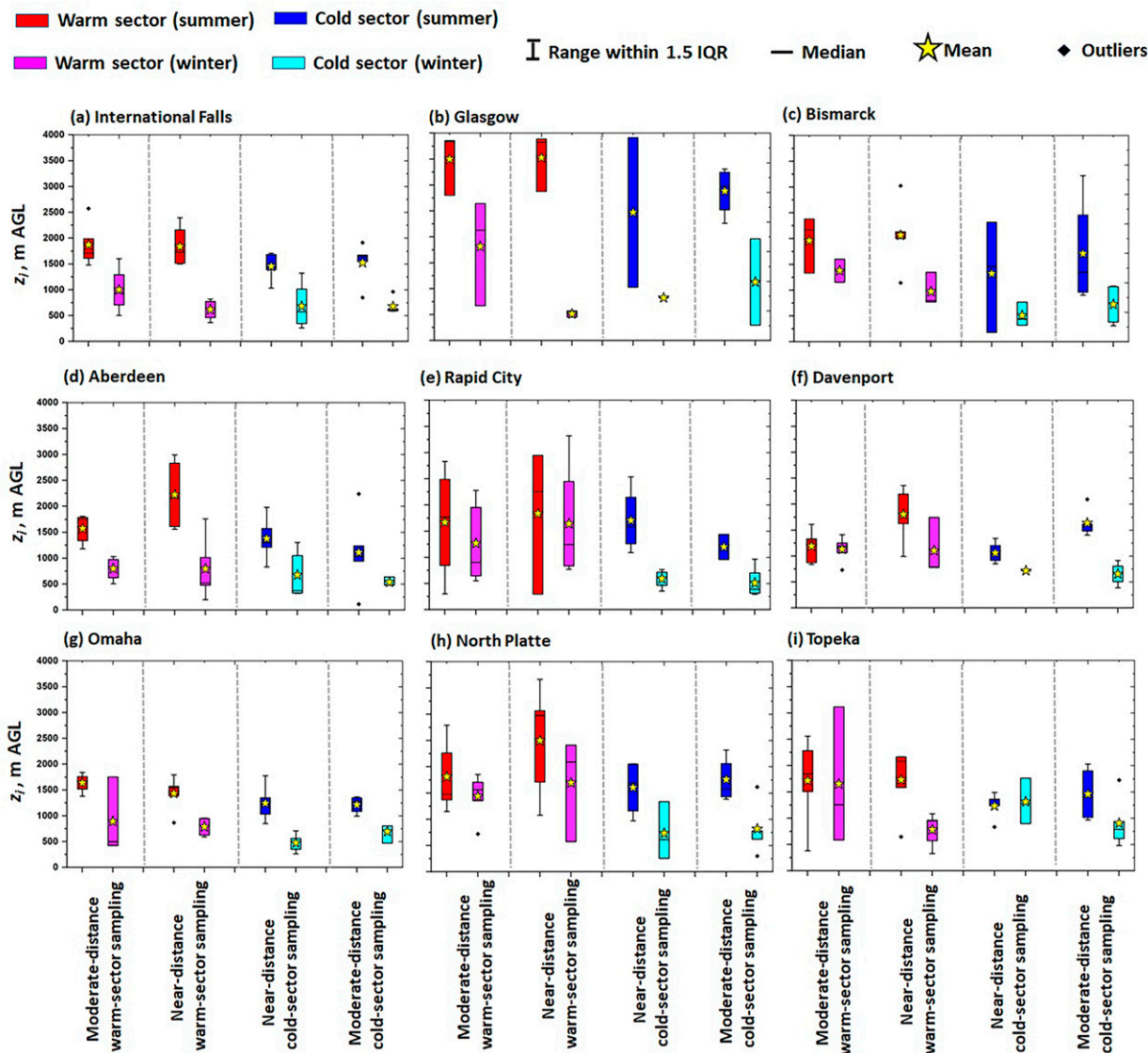


FIG. C1. Box-and-whisker plots of z_i variability across frontal boundaries (i.e., z_i in warm vs cold sectors) observed for the 5-yr period during summer (red and blue boxes for warm- and cold-sector z_i samples, respectively) and winter (magenta and cyan boxes for warm- and cold-sector z_i samples, respectively) at the 9 IGRA sites [from north to south: (a) International Falls, (b) Glasgow, (c) Bismarck, (d) Aberdeen, (e) Rapid City, (f) Davenport, (g) Omaha, (h) North Platte, and (i) Topeka; see Table A1 in appendix A for locations] illustrating overall front-relative and site-specific z_i variability during summer and winter. The symbols and other parameters that appear in the box-and-whisker plots are identical to symbols presented in Fig. 7, except the yellow stars represent the means.

showed that significant horizontal airmass gradients caused by the frontal passage modulate z_i and provide an essential perspective for the boundary layer meteorology community involved in observing and simulating ABL parameters.

Our work also showed the potential of routine rawinsonde measurements to derive front-relative z_i -variability over multiple sites during two contrasting seasons (summer and winter). The method could be used for high-resolution measurements from other ground-based remote sensing instruments (An et al. 2019), ground-based lidar networks (Lewis et al. 2013), and airborne sensors in a frontal environment (Pal 2019; Pal et al. 2020a). In the future, we plan to extend this research by

analyzing airborne lidar measurements of z_i (Pal et al. 2020a) and in situ profiles of thermodynamic profiles (Pal 2019) across frontal passages obtained during recent field campaigns (e.g., Davis et al. 2021). Using airborne meteorological measurements, we can further advance our understanding of the role of horizontal advection on z_i spatial variability across frontal boundaries. Although the method introduced to determine front-relative z_i features work in a semiautomated fashion, we argue that future work will be helpful to improve the method, making it objective and automated. Nevertheless, this work is a starting point for obtaining comprehensive details on

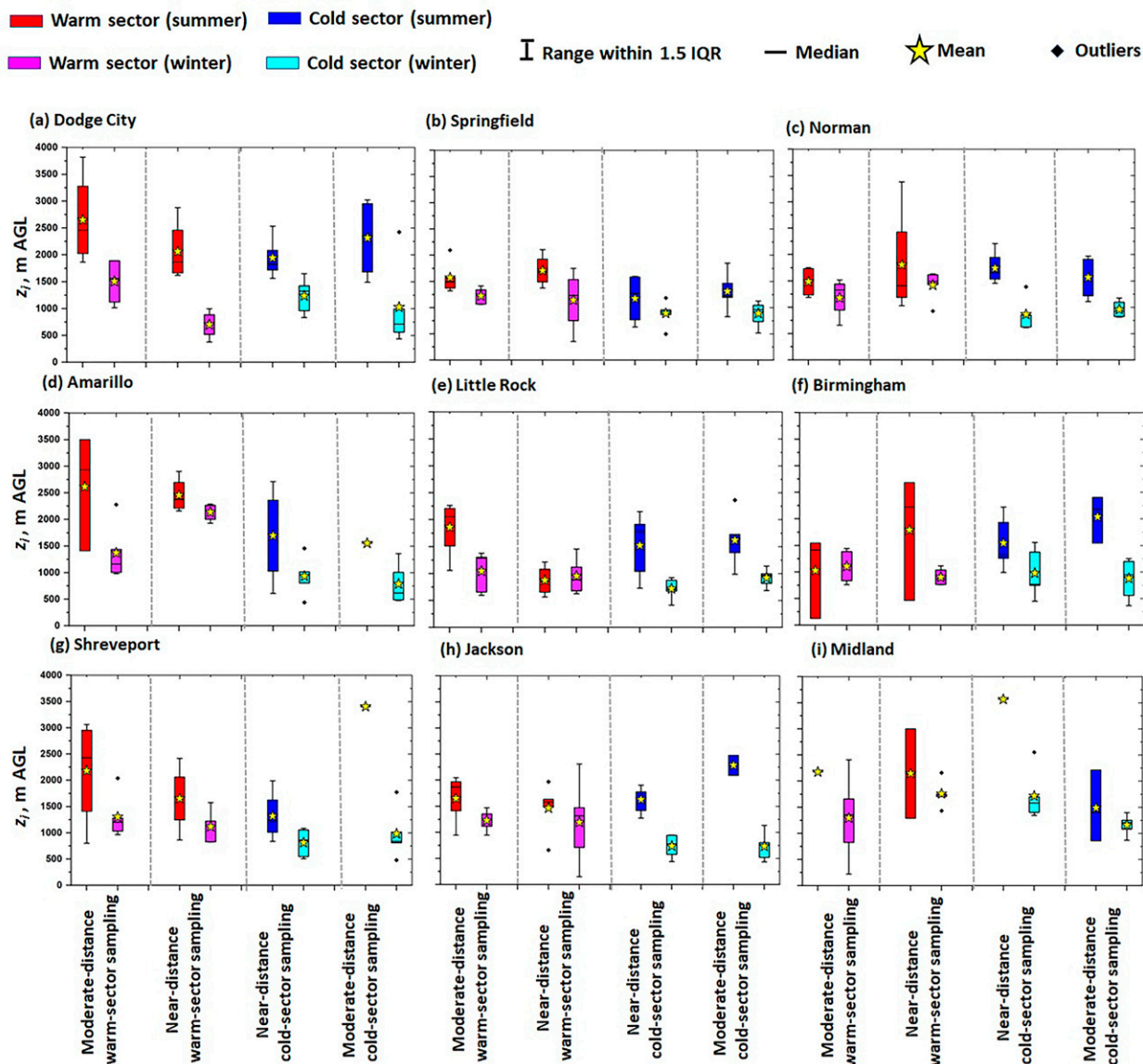


FIG. C2. As in Fig. C1, but for the other 9 IGRA sites: (a) Dodge City, (b) Springfield, (c) Norman, (d) Amarillo, (e) Little Rock, (f) Birmingham, (g) Shreveport, (h) Jackson, and (i) Midland; see Table A1 in appendix A for locations.

the impact of frontal passages on z_i variability in the future via using both ground-based and airborne lidar observations in frontal environment (Pal et al. 2021).

The observational findings reported here could be compared with NARR and HRRR simulations (e.g., Mesinger et al. 2006; Benjamin et al. 2016) to investigate the performance of state-of-the-art high-resolution models to determine whether these models can capture the frontal modifications of z_i . Future work using NARR, high-resolution NWP models, or HRRR output will provide additional information on the variability and relative contributions of buoyancy and shear across frontal boundaries.

Acknowledgments. The corresponding author Pal was supported by the Texas Tech University Faculty Start-up Funds and NASA Grant 80NSSC19K0730, and coauthor Clark was

funded by the Program in Inquiry and Investigation: Pi2 program in Texas Tech University. We note that all results and conclusions of this study, as well as any views expressed herein, are those of the authors and do not necessarily reflect those of NOAA or the Department of Commerce. We also thank the three anonymous referees for their objective assessments and constructive criticisms. Their time and effort should be considered an excellent turning point of this work and the basis for the many significant improvements that went into the paper during the revisions.

Data availability statement. The IGRA rawinsonde datasets (<https://www.ncdc.noaa.gov/data-access/weather-balloon/integrated-global-radiosonde-archive>) and the WPC surface charts (<https://www.wpc.ncep.noaa.gov/archives/sfc/>) were obtained online.

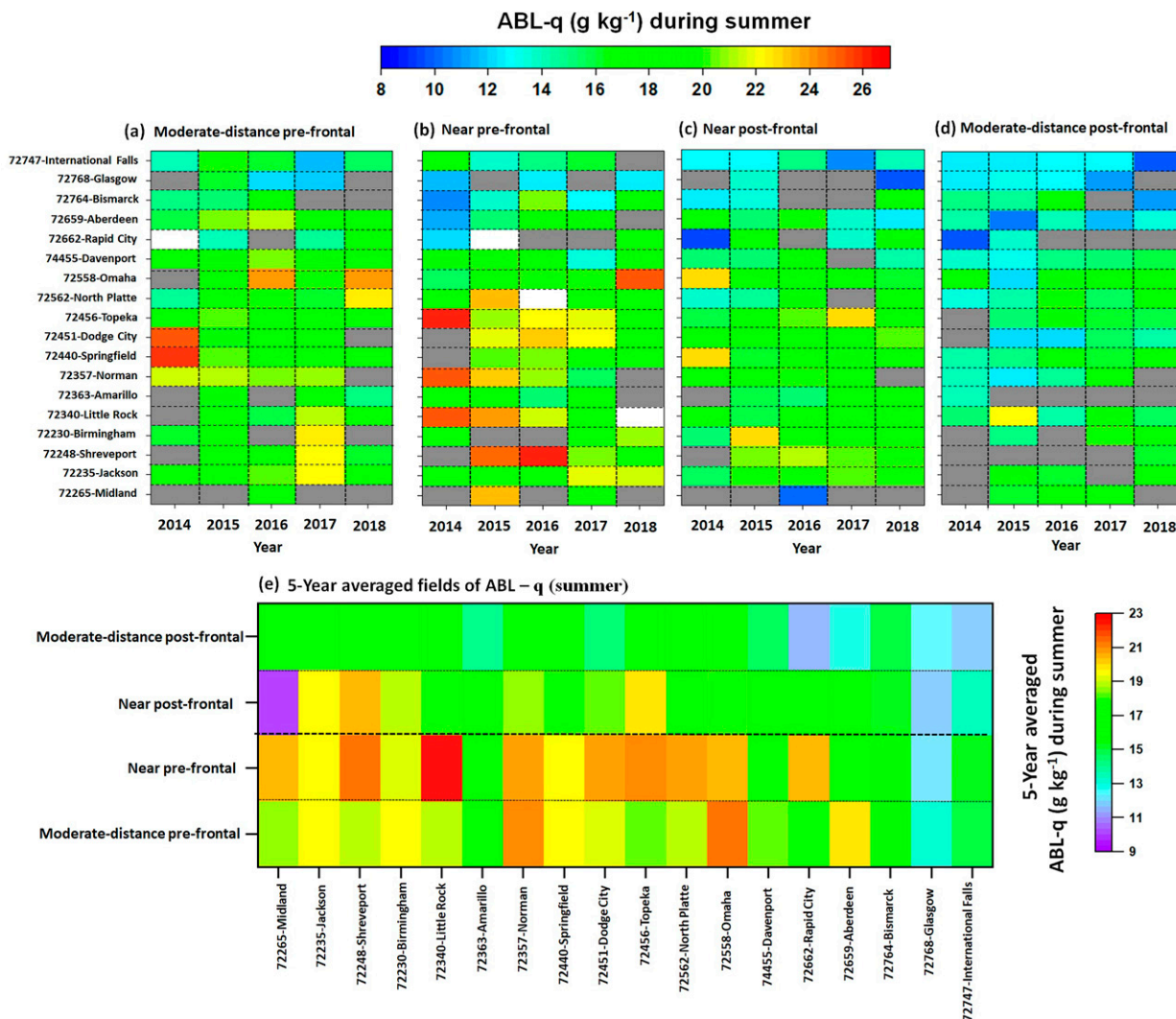


FIG. D1. Heat-map view of summertime ABL- q over the 18 IGRA sites during sampling times for the regimes identified as (a) moderate-distance prefrontal, (b) near prefrontal, (c) near postfrontal, and (d) moderate-distance postfrontal. Also shown is (e) a 5-yr-averaged field yielding overall prefrontal vs postfrontal ABL- q variability for both moderate- and near-distance samplings. The color-bar scale limit in (e) is kept different than in the other panels to show the overall cross-frontal ABL- q variability. The sites are arranged from south to north along the y axis by latitude. Gray pixels denote gaps in pre- or postfrontal sampling of ABL- q . A few pixels in (a) and (b) are kept saturated (i.e., ABL- q of more than 27 g kg^{-1}) to yield the contrasts between the warm [(a) and (b)] and cold [(c) and (d)] sectors.

APPENDIX A

Locations of the IGRA Sites

Table A1 provides brief information about the locations of the rawinsonde sites selected for this study.

APPENDIX B

Overall Number of Frontal Passages over the 18 IGRA Stations

This appendix presents an overview of the number of frontal passages over the IGRA sites when z_i measurements were available for both moderate- and near-distance ABL frontal sampling for the 5-yr period (Fig. B1).

APPENDIX C

Variability in z_i across Frontal Boundaries

Figures C1 and C2 provide an overview of z_i changes due to frontal passages at the 18 IGRA sites during both summer and winter for the 5-yr period using box-and-whisker plots of z_i variability yielding site-specific z_i frontal contrasts (i.e., Δz_i features).

APPENDIX D

Boundary Layer Moisture and Potential Temperature across Frontal Boundaries

Heat-map views of ABL- q (g kg^{-1}) over the 18 IGRA sites during summer (Fig. D1) and winter (Fig. D2) yielded

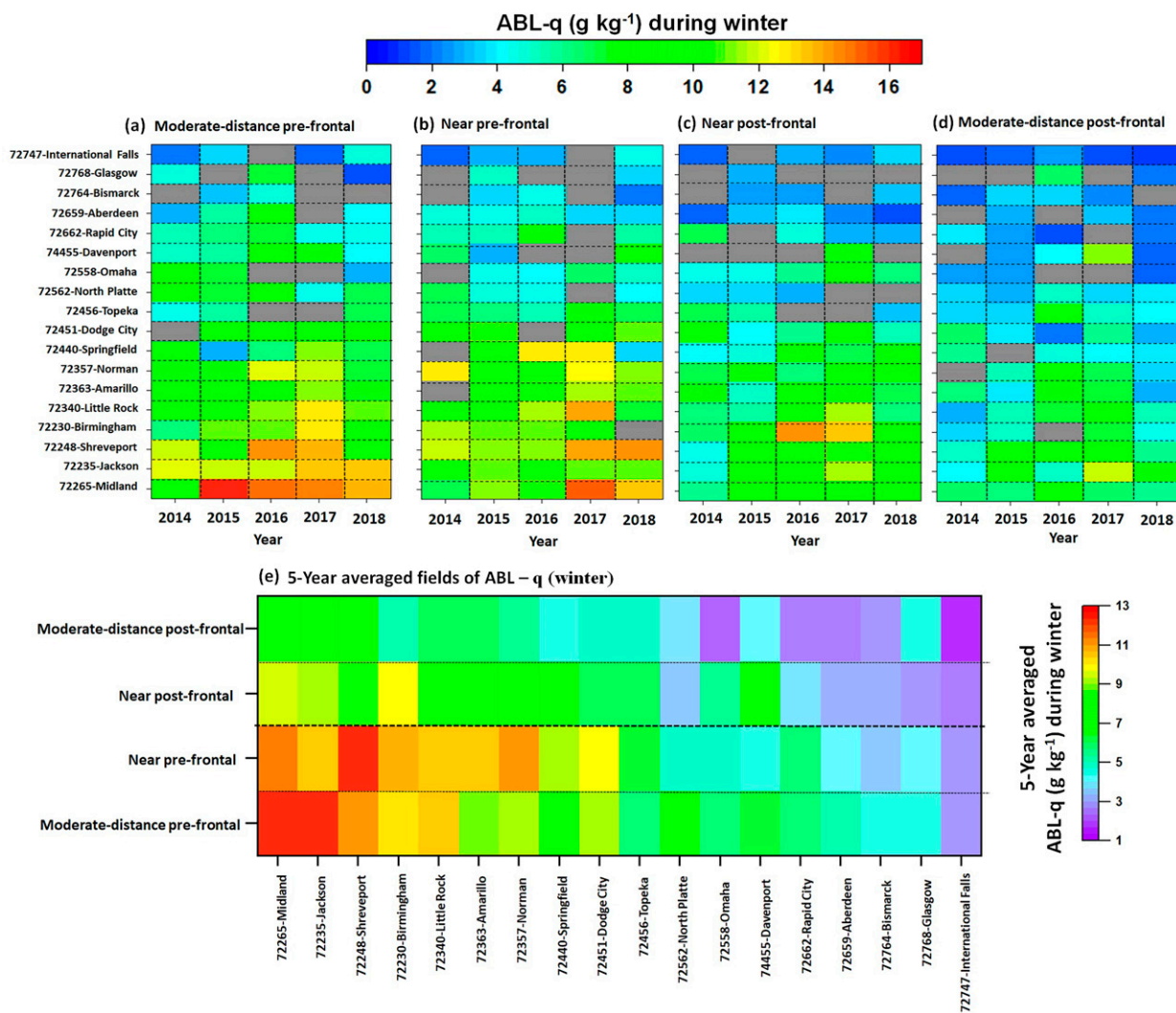


FIG. D2. As in Fig. D1, but for $ABL-q$ ($g\ kg^{-1}$) during winter. Color-bar scale limits of $ABL-q$ are kept different than used in Fig. D1 to compare $ABL-q$ between the warm- and cold-sector ABL regimes in winter and not meant to compare $ABL-q$ between summer and winter.

typical frontal signatures in $ABL-q$ (i.e., a relatively more humid warm sector than cold sector). Similar analyses of $ABL-\theta$ (K) for summer (Fig. D3) and winter (Fig. D4) also underscored the typical differences in $ABL-\theta$ across frontal boundaries over land. The potential temperature and moisture variability in the warm and cold sectors and their differences provided strong support to the typical frontal signatures on ABL thermodynamics and helps to demonstrate the method introduced for determining frontal signatures in z_r .

APPENDIX E

A Step-by-Step Guide for Using the Shell Script to Automatically Obtain Surface Map Analyses

For the purposes of conducting this research, we utilized Windows as the preferred choice of operating system (OS)

and, as such, we described below the steps necessary to execute script using Windows OS. We note, however, that other OS (i.e., Linux and Mac) have different built-in commands; thus, many of the steps in this guide may be excluded.

- Step 1: Windows OS has none of the built-in functions necessary to execute the Shell Script described in this work and, hence, using the Command Prompt will be avoided for ease of use. Instead, we recommend either Git Bash (<https://git-scm.com/download/win>) or Cygwin (<https://www.cygwin.com/install.html>) to be used as the main shell for executing the script. During this process, it will be convenient if the users can remember the local directory in which the shell is installed. We note that during the installation of the Cygwin Terminal, the users are encouraged to install the “wget” package (wget-1.21-1) when prompted. Otherwise, users should continue the steps in order as below.

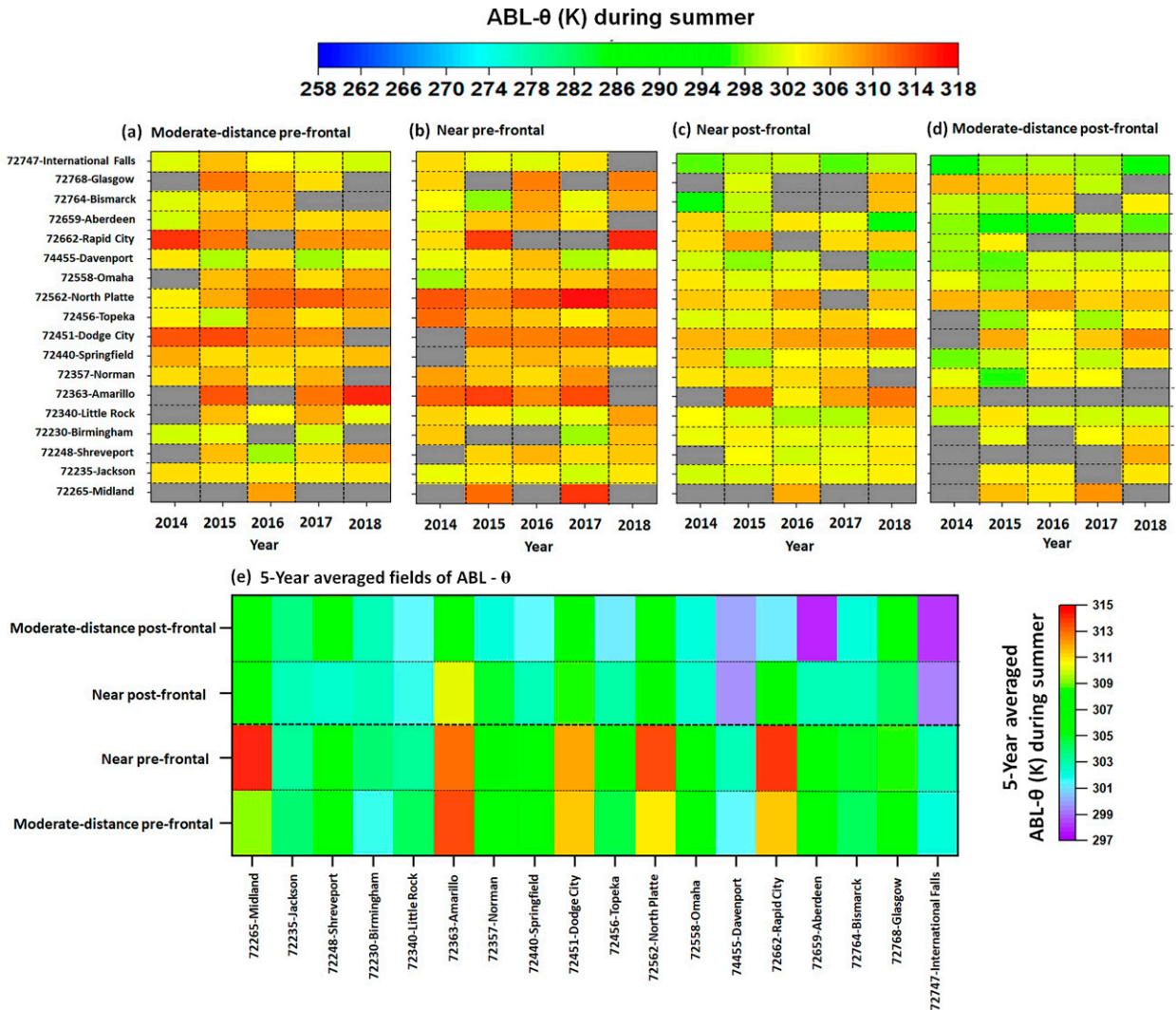


FIG. D3. As in Fig. D2, but for ABL- θ (K) during summer during the period 2014–18.

- Step 2: After installing Git Bash or Cygwin, download either the 32- or 64-bit most-up-to-date version of “wget.exe” from GNU Wget 1.21.1 for Windows (eternallybored.org) (available at <https://eternallybored.org/misc/wget/>). On the website, there are also .zip binary files that may be used instead. However, for simplicity, the .exe file will suffice to properly execute the script.
- Step 3: After downloading the wget.exe application, return to the directory in which either Git Bash or Cygwin was installed. Copy and paste the installed wget.exe file into either the ... \mingw64\bin or ... \bin folder for Git Bash and Cygwin, respectively. Then, run the application (required step). If done appropriately, when “wget -h” is typed into the command line, a list of options should appear.
- Step 4: At this point, the code should have all the necessary functions to run. In either Git Bash or Cygwin, change directories using the “cd” command to the address in which the code is stored. For example, “cd ‘C:\Users\User\Scripts’”.

Then, use the built-in “bash” command to run the script, for example, bash ‘script.sh’. Note that the file extension for the script is “.sh”. The code will then retrieve the appropriate URL address (see below).

Note that, for the purposes of this work, we retrieved surface synoptic maps that are stored in an archive directory online and have the following general URL address format: <https://www.wpc.ncep.noaa.gov/archives/sfc/{year}/usfntsfc{year}{month}{day}{UTC}.gif>, where the year, month, day, and UTC variables should be exchanged for a desired time—for instance, <https://www.wpc.ncep.noaa.gov/archives/sfc/2015/usfntsfc2015071615.gif>. Note that these values are zero padded (e.g., YYYYMMDDHH for a date, where the letters are the placeholders for year, month, day, and hour). Note also that this process works for any file type stored in any archive with minor adjustments to the code. For instance, this script could be used to retrieve different types of maps stored in the NOAA archive

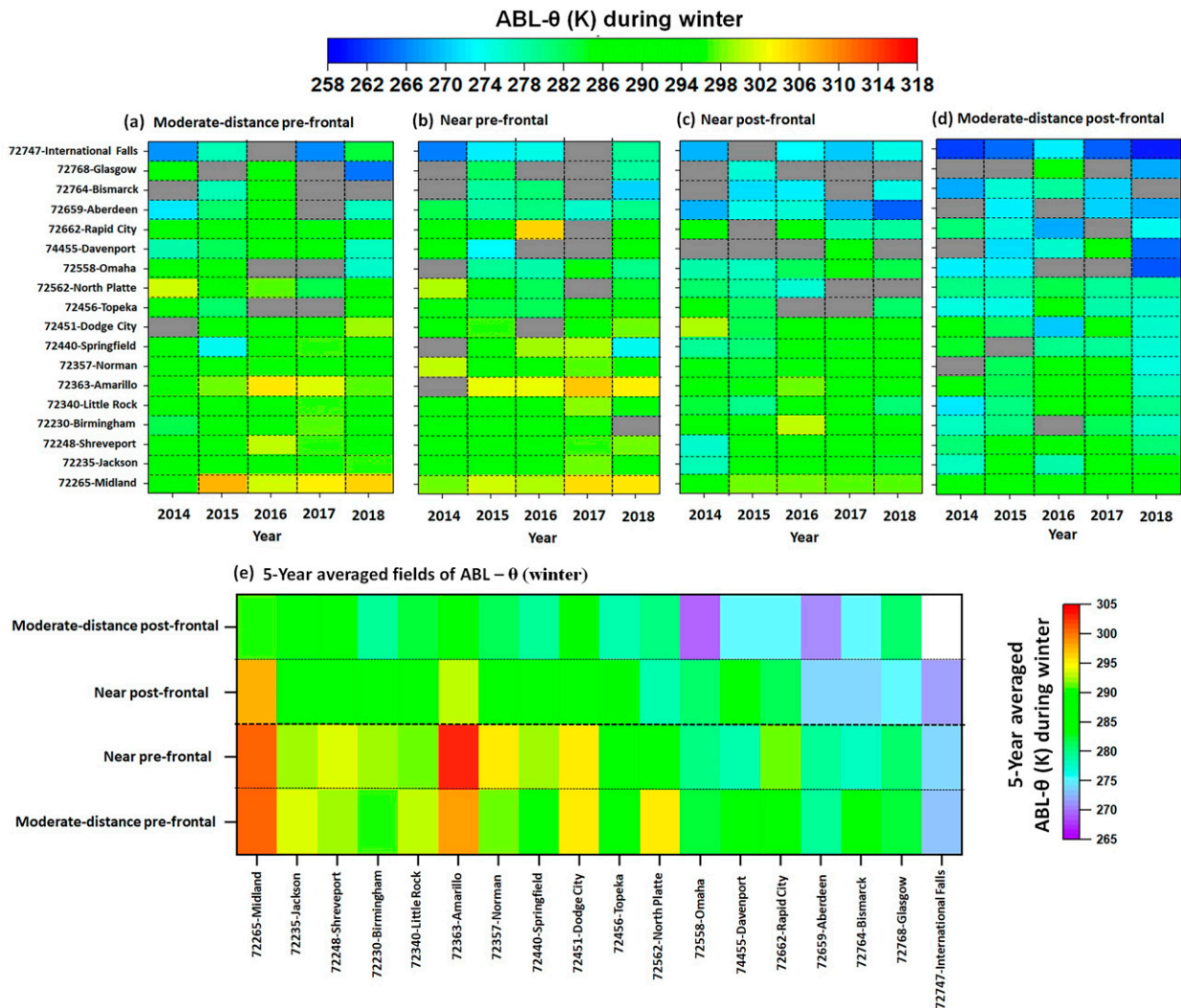


FIG. D4. As in Fig. D3, but for ABL- θ (K) during winter. Also, color-bar scale limits of ABL- θ are kept identical here to compare front-relative changes in ABL- θ between summer and winter.

(https://www.wpc.ncep.noaa.gov/archives/sfc/2015/radsfcus_exp2015071615.gif) or even ASOS data (<https://www.ncei.noaa.gov/pub/data/asos-fivemin/6401-2015/64010K1J0201506.dat>) if the URL address is known in advance.

REFERENCES

- An, N., R. T. Pinker, K. Wang, E. Rogers, and Z. Zuo, 2019: Evaluation of cloud base height in the North American Regional Reanalysis using ceilometer observations. *Int. J. Climatol.*, **40**, 3161–3178, <https://doi.org/10.1002/joc.6389>.
- Angevine, W. M., A. B. White, C. J. Senff, M. Trainer, R. M. Banta, and M. A. Ayoub, 2003: Urban–rural contrasts in mixing height and cloudiness over Nashville in 1999. *J. Geophys. Res.*, **108**, 4092, <https://doi.org/10.1029/2001JD001061>.
- Barlow, J. F., 2014: Progress in observing and modelling the urban boundary layer. *Urban Climate*, **10**, 216–240, <https://doi.org/10.1016/j.uclim.2014.03.011>.
- Benjamin, S. G., and Coauthors, 2016: A North American hourly assimilation and model forecast cycle: The Rapid Refresh. *Mon. Wea. Rev.*, **144**, 1669–1694, <https://doi.org/10.1175/MWR-D-15-0242.1>.
- Berry, G., M. J. Reeder, and C. Jakob, 2011: A global climatology of atmospheric fronts. *Geophys. Res. Lett.*, **38**, L04809, <https://doi.org/10.1029/2010GL046451>.
- Bethan, S., G. Vaughan, C. Gerbig, A. Volz-Thomas, H. Richer, and D. A. Tiddeman, 1998: Chemical air mass differences near fronts. *J. Geophys. Res.*, **103**, 13 413–13 434, <https://doi.org/10.1029/98JD00535>.
- Bond, N. A., and R. G. Fleagle, 1988: Pre-frontal and post-frontal boundary layer processes over the ocean. *Mon. Wea. Rev.*, **116**, 1257–1273, [https://doi.org/10.1175/1520-0493\(1988\)116<1257:PAPBLP>2.0.CO;2](https://doi.org/10.1175/1520-0493(1988)116<1257:PAPBLP>2.0.CO;2).
- Boutle, I. A., S. E. Belcher, and R. S. Plant, 2011: Moisture transport in mid-latitude cyclones. *Quart. J. Roy. Meteor. Soc.*, **137**, 360–373, <https://doi.org/10.1002/qj.783>.

- Browning, K. A., 1997: The dry intrusion perspective of extra-tropical cyclone development. *Meteor. Appl.*, **4**, 317–324, <https://doi.org/10.1017/S1350482797000613>.
- , M. E. Hardman, T. W. Harrold, and C. W. Pardoc, 1973: The structure of rainbands within a mid-latitude depression. *Quart. J. Roy. Meteor. Soc.*, **99**, 215–231, <https://doi.org/10.1002/qj.49709942002>.
- Carlson, T. N., 1980: Airflow through midlatitude cyclones and the comma cloud pattern. *Mon. Wea. Rev.*, **108**, 1498–1509, [https://doi.org/10.1175/1520-0493\(1980\)108<1498:ATMCAT>2.0.CO;2](https://doi.org/10.1175/1520-0493(1980)108<1498:ATMCAT>2.0.CO;2).
- Cooper, O. R., and Coauthors, 2004: A case study of transpacific warm conveyor belt transport: Influences of merging airstream on trace gas import to North America. *J. Geophys. Res.*, **109**, D23S08, <https://doi.org/10.1029/2003JD003624>.
- Davis, K. J., and Coauthors, 2021: The Atmospheric Carbon and Transport (ACT)–America Mission. *Bull. Amer. Meteor. Soc.*, **102**, E1714–E1734, <https://doi.org/10.1175/BAMS-D-20-0300.1>.
- Davis, R. E., and L. S. Kalkstein, 1990: Development of an automated spatial synoptic climatological classification. *Int. J. Climatol.*, **10**, 769–794, <https://doi.org/10.1002/joc.3370100802>.
- , B. P. Hayden, D. A. Gay, W. L. Phillips, and G. V. Jones, 1997: The North Atlantic subtropical anticyclone. *J. Climate*, **10**, 728–744, [https://doi.org/10.1175/1520-0442\(1997\)010<0728:TNASA>2.0.CO;2](https://doi.org/10.1175/1520-0442(1997)010<0728:TNASA>2.0.CO;2).
- DiMego, G. J., L. F. Bosart, and G. W. Endersen, 1976: An examination of the frequency and mean conditions surrounding frontal incursions into the Gulf of Mexico and Caribbean Sea. *Mon. Wea. Rev.*, **104**, 709–718, [https://doi.org/10.1175/1520-0493\(1976\)104<0709:AEOTFA>2.0.CO;2](https://doi.org/10.1175/1520-0493(1976)104<0709:AEOTFA>2.0.CO;2).
- Dolan, R., and R. E. Davis, 1992: An intensity scale for Atlantic coast northeast storms. *J. Coast. Res.*, **8**, 840–853.
- Doswell, C. A., III, and M. J. Haugland, 2007: A comparison of two cold fronts—Effects of the planetary boundary layer on the mesoscale. *Electron. J. Severe Storms Meteor.*, **2** (4), <https://ejssm.org/archives/wp-content/uploads/2021/09/vol2-4.pdf>.
- Durre, I., and X. Yin, 2008: Enhanced radiosonde data for studies of vertical structure. *Bull. Amer. Meteor. Soc.*, **89**, 1257–1262, <https://doi.org/10.1175/2008BAMS2603.1>.
- Emeis, S., C. Jahn, C. Münkel, C. Münsterer, and K. Schäfer, 2007: Multiple atmospheric layering and mixing-layer height in the Inn Valley observed by remote sensing. *Meteor. Z.*, **16**, 415–424, <https://doi.org/10.1127/0941-2948/2007/0203>.
- Engelbart, D. A. M., M. Kallistratova, and R. Kouznetsov, 2007: Determination of the turbulent fluxes of heat and momentum in the ABL by ground-based remote-sensing techniques (a review). *Meteor. Z.*, **16**, 325–335, <https://doi.org/10.1127/0941-2948/2007/0224>.
- Harvey, B., J. Methven, C. Eagle, and H. Lean, 2017: Does the representation of flow structure and turbulence at a cold front converge on multiscale observations with model resolution? *Mon. Wea. Rev.*, **145**, 4345–4363, <https://doi.org/10.1175/MWR-D-16-0479.1>.
- Heaviside, C., X.-M. Cai, and S. Vardoulakis, 2015: The effects of horizontal advection on the urban heat island in Birmingham and the West Midlands, United Kingdom during a heatwave. *Quart. J. Roy. Meteor. Soc.*, **141**, 1429–1441, <https://doi.org/10.1002/qj.2452>.
- Hoch, J., and P. Markowski, 2005: A climatology of springtime dryline position in the U.S. Great Plains region. *J. Climate*, **18**, 2132–2137, <https://doi.org/10.1175/JCLI3392.1>.
- Hoskins, B. J., and F. P. Bretherton, 1972: Atmospheric frontogenesis models: Mathematical formulation and solution. *J. Atmos. Sci.*, **29**, 11–37, [https://doi.org/10.1175/1520-0469\(1972\)029<0011:AFMMFA>2.0.CO;2](https://doi.org/10.1175/1520-0469(1972)029<0011:AFMMFA>2.0.CO;2).
- Ilotoviz, E., V. P. Ghate, and S. Raveh-Rubin, 2021: The impact of slantwise descending dry intrusions on the marine boundary layer and air-sea interface over the ARM Eastern North Atlantic site. *J. Geophys. Res. Atmos.*, **126**, e2020JD033879, <https://doi.org/10.1029/2020JD033879>.
- Janjic, Z., and R. Gall, 2012: Scientific documentation of the NCEP Nonhydrostatic Multiscale Model on the B grid (NMMB)—Part 1: Dynamics. NCAR Tech. Note NCAR/TN-489+STR, 80 pp., <https://doi.org/10.5065/D6WH2MZX>.
- Kaimal, J., and J. Finnigan, 1994: *Atmospheric Boundary Layer Flows: Their Structure and Measurement*. Oxford University Press, 304 pp.
- Koffi, E. N., and Coauthors, 2016: Evaluation of the boundary layer dynamics of the TM5 model over Europe. *Geosci. Model Dev.*, **9**, 3137–3160, <https://doi.org/10.5194/gmd-9-3137-2016>.
- Lee, T. R., and S. F. J. De Wekker, 2016: Estimating daytime planetary boundary layer heights over a valley from rawinsonde observations at a nearby airport: An application to the Page Valley in Virginia, United States. *J. Appl. Meteor. Climatol.*, **55**, 791–809, <https://doi.org/10.1175/JAMC-D-15-0300.1>.
- , and S. Pal, 2017: On the potential of 25 years (1991–2015) of rawinsonde measurements for elucidating key climatological and spatiotemporal patterns of afternoon boundary layer depths over the contiguous US. *Adv. Meteor.*, **2017**, 6841239, <https://doi.org/10.1155/2017/6841239>.
- , and —, 2020: The impact of height-independent errors in state variables on the determination of the daytime atmospheric boundary layer depth using the bulk Richardson approach. *J. Atmos. Oceanic Technol.*, **38**, 47–61, <https://doi.org/10.1175/JTECH-D-20-0135.1>.
- , S. F. J. De Wekker, A. E. Andrews, J. Kofler, and J. Williams, 2012: Carbon dioxide variability during cold front passages and fair weather days at a forested mountaintop site. *Atmos. Environ.*, **46**, 405–416, <https://doi.org/10.1016/j.atmosenv.2011.09.068>.
- , —, S. Pal, A. E. Andrews, and J. Kofler, 2015: Meteorological controls on the diurnal variability of carbon monoxide mixing ratio at a mountaintop monitoring site in the Appalachian Mountains. *Tellus*, **67B**, 25659, <https://doi.org/10.3402/tellus.v67.25659>.
- , —, and —, 2018: The impact of the afternoon planetary boundary-layer height on the diurnal cycle of CO and CO₂ mixing ratios at a low-altitude mountaintop. *Bound.-Layer Meteor.*, **168**, 81–102, <https://doi.org/10.1007/s10546-018-0343-9>.
- LeMone, M. A., and Coauthors, 2019: 100 years of progress in boundary layer meteorology. *A Century of Progress in Atmospheric and Related Sciences: Celebrating the American Meteorological Society Centennial*, *Meteor. Monogr.*, No. 59, Amer. Meteor. Soc., <https://doi.org/10.1175/AMSMONOGRAPHS-D-18-0013.1>.
- Lenschow, D. H., 1973: Two examples of planetary boundary layer modification over the Great Lakes. *J. Atmos. Sci.*, **30**, 568–581, [https://doi.org/10.1175/1520-0469\(1973\)030<0568:TEOPBL>2.0.CO;2](https://doi.org/10.1175/1520-0469(1973)030<0568:TEOPBL>2.0.CO;2).
- Lewis, J. R., E. J. Welton, A. M. Molod, and E. Joseph, 2013: Improved boundary layer depth retrievals from MPLNET. *J. Geophys. Res. Atmos.*, **118**, 9870–9879, <https://doi.org/10.1002/jgrd.50570>.
- Li, L., W. Li, and Y. Kushnir, 2011: Variation of North Atlantic subtropical high western ridge and its implications to the southeastern US summer precipitation. *Climate Dyn.*, **39**, 1401–1412, <https://doi.org/10.1007/s00382-011-1214-y>.

- Lopez-Coto, I., M. Hicks, A. Karion, R. K. Sakai, B. Demoz, K. Prasad, and J. Whetstone, 2020: Assessment of planetary boundary layer parametrizations and urban heat island comparison: Impacts and implications for tracer transport. *J. Appl. Meteor. Climatol.*, **59**, 1637–1653, <https://doi.org/10.1175/JAMC-D-19-0168.1>.
- Mahrt, L., 1991: Boundary-layer moisture regimes. *Quart. J. Roy. Meteor. Soc.*, **117**, 151–176, <https://doi.org/10.1002/qj.49711749708>.
- Markowski, P., and Y. Richardson, 2010: *Mesoscale Meteorology in Midlatitudes*. John Wiley and Sons, 407 pp.
- Medeiros, B., A. Hall, and B. Stevens, 2005: What controls the mean depth of the PBL? *J. Climate*, **18**, 3157–3172, <https://doi.org/10.1175/JCLI3417.1>.
- Mesinger, F., and Coauthors, 2006: North American Regional Reanalysis. *Bull. Amer. Meteor. Soc.*, **87**, 343–360, <https://doi.org/10.1175/BAMS-87-3-343>.
- National Academies of Sciences, Engineering, and Medicine, 2018: *The Future of Atmospheric Boundary Layer Observing, Understanding, and Modeling: Proceedings of a Workshop*. National Academies Press, 58 pp., <https://doi.org/10.17226/25138>.
- Naud, C., J. Booth, and A. Del Genio, 2016: The relationship between boundary layer stability and cloud cover in the post-cold-frontal region. *J. Climate*, **29**, 8129–8149, <https://doi.org/10.1175/JCLI-D-15-0700.1>.
- Neiman, P. J., F. M. Ralph, M. A. Shapiro, B. F. Smull, and D. Johnson, 1998: An observational study of fronts and frontal mergers over the continental United States. *Mon. Wea. Rev.*, **126**, 2521–2554, [https://doi.org/10.1175/1520-0493\(1998\)126<2521:AOSOFA>2.0.CO;2](https://doi.org/10.1175/1520-0493(1998)126<2521:AOSOFA>2.0.CO;2).
- Pal, S., 2014: Monitoring depth of shallow atmospheric boundary layer to complement lidar measurements affected by partial overlap. *Remote Sens.*, **6**, 8468–8493, <https://doi.org/10.3390/rs6098468>.
- , 2019: ACT-America: Profile-based Planetary Boundary Layer Heights, Eastern USA. ORNL DAAC, accessed 20 June 2021, <https://doi.org/10.3334/ORNLDAAC/1706>.
- , and M. Haefelin, 2015: Forcing mechanisms governing diurnal, seasonal, and inter-annual variability in the boundary layer depths: Five years of continuous lidar observations over a suburban site near Paris. *J. Geophys. Res. Atmos.*, **120**, 11 936–11 956, <https://doi.org/10.1002/2015JD023268>.
- , and T. R. Lee, 2019a: Contrasting air mass advection explains significant differences in boundary layer depth seasonal cycles under onshore versus offshore flows. *Geophys. Res. Lett.*, **46**, 2846–2853, <https://doi.org/10.1029/2018GL081699>.
- , and —, 2019b: Advected air mass reservoirs in the downwind of mountains and their roles in overrunning boundary layer depths over the plains. *Geophys. Res. Lett.*, **46**, 10 140–10 149, <https://doi.org/10.1029/2019GL083988>.
- , S. F. J. De Wekker, and G. D. Emmitt, 2016: Investigation of the spatial variability of the convective boundary layer heights over an isolated mountain: Cases from the MATERHORN-2012 experiment. *J. Appl. Meteor. Climatol.*, **55**, 1927–1952, <https://doi.org/10.1175/JAMC-D-15-0277.1>.
- , and Coauthors, 2020a: Observations of greenhouse gas changes across summer frontal boundaries in the eastern United States. *J. Geophys. Res. Atmos.*, **125**, e2019JD030526, <https://doi.org/10.1029/2019JD030526>.
- , T. R. Lee, and N. E. Clark, 2020b: The 2019 Mississippi and Missouri River flooding and its impact on atmospheric boundary layer dynamics. *Geophys. Res. Lett.*, **47**, e2019GL086933, <https://doi.org/10.1029/2019GL086933>.
- , and Coauthors, 2021: ACT-America: CPL-derived Atmospheric Boundary Layer Top Height, Eastern US, 2016–2018. ORNL DAAC, accessed 20 July 2021, <https://doi.org/10.3334/ORNLDAAC/1825>.
- Parsons, D. B., M. A. Shapiro, R. M. Hardesty, R. J. Zamora, and J. M. Intrieri, 1991: The finescale structure of a West Texas dryline. *Mon. Wea. Rev.*, **119**, 1242–1258, [https://doi.org/10.1175/1520-0493\(1991\)119<1242:TFSOAW>2.0.CO;2](https://doi.org/10.1175/1520-0493(1991)119<1242:TFSOAW>2.0.CO;2).
- Payer, M., N. F. Laird, R. J. Maliawco, and E. G. Hoffman, 2011: Surface fronts, troughs, and baroclinic zones in the Great Lakes region. *Wea. Forecasting*, **26**, 555–563, <https://doi.org/10.1175/WAF-D-10-05018.1>.
- Persson, P. O. G., J. E. Hare, C. W. Fairall, and W. D. Otto, 2005: Air-sea interaction processes in warm and cold sectors of extratropical cyclonic storms observed during FASTEX. *Quart. J. Roy. Meteor. Soc.*, **131**, 877–912, <https://doi.org/10.1256/qj.03.181>.
- Purvis, R., and Coauthors, 2003: Rapid uplift of nonmethane hydrocarbons in a cold front over central Europe. *J. Geophys. Res.*, **108**, 4224, <https://doi.org/10.1029/2002JD002521>.
- Rotach, M. W., and Coauthors, 2022: A collaborative effort to better understand, measure and model atmospheric exchange processes over mountains. *Bull. Amer. Meteor. Soc.*, **103**, E1282–E1295, <https://doi.org/10.1175/BAMS-D-21-0232.1>.
- Sanders, F., and C. A. Doswell, 1995: A case study for detailed surface analysis. *Bull. Amer. Meteor. Soc.*, **76**, 505–521, [https://doi.org/10.1175/1520-0477\(1995\)076<0505:ACFDSA>2.0.CO;2](https://doi.org/10.1175/1520-0477(1995)076<0505:ACFDSA>2.0.CO;2).
- Seibert, P., F. Beyrich, S.-E. Gryning, S. Joffre, A. Rasmussen, and P. Tercier, 2000: Review and intercomparison of operational methods for the determination of the mixing height. *Atmos. Environ.*, **34**, 1001–1027, [https://doi.org/10.1016/S1352-2310\(99\)00349-0](https://doi.org/10.1016/S1352-2310(99)00349-0).
- Seidel, D. J., C. O. Ao, and K. Li, 2010: Estimating climatological planetary boundary layer heights from radiosonde observations: Comparison of methods and uncertainty analysis. *J. Geophys. Res.*, **115**, D16113, <https://doi.org/10.1029/2009JD013680>.
- , Y. Zhang, A. Beljaars, J.-C. Golaz, A. R. Jacobson, and B. Medeiros, 2012: Climatology of the planetary boundary layer over the continental United States and Europe. *J. Geophys. Res.*, **117**, D17106, <https://doi.org/10.1029/2012JD018143>.
- Shafer, J. C., and W. J. Steenburgh, 2008: Climatology of strong Intermountain cold fronts. *Mon. Wea. Rev.*, **136**, 784–807, <https://doi.org/10.1175/2007MWR2136.1>.
- Sinclair, V. A., 2013: A 6-yr climatology of fronts affecting Helsinki, Finland, and their boundary layer structure. *J. Appl. Meteor. Climatol.*, **52**, 2106–2124, <https://doi.org/10.1175/JAMC-D-12-0318.1>.
- , S. L. Gray, and S. E. Belcher, 2008: Boundary-layer ventilation by baroclinic life cycles. *Quart. J. Roy. Meteor. Soc.*, **134**, 1409–1424, <https://doi.org/10.1002/qj.293>.
- , S. E. Belcher, and S. L. Gray, 2010: Synoptic controls on boundary-layer characteristics. *Bound.-Layer Meteor.*, **134**, 387–409, <https://doi.org/10.1007/s10546-009-9455-6>.
- , S. Niemelä, and M. Leskinen, 2012: Structure of a narrow cold front in the boundary layer: Observations versus model simulation. *Mon. Wea. Rev.*, **140**, 2497–2519, <https://doi.org/10.1175/MWR-D-11-00328.1>.
- Stensrud, D. J., 1993: Elevated residual layers and their influence on surface boundary layer evolution. *J. Atmos. Sci.*, **50**, 2284–2293, [https://doi.org/10.1175/1520-0469\(1993\)050<2284:ERLATI>2.0.CO;2](https://doi.org/10.1175/1520-0469(1993)050<2284:ERLATI>2.0.CO;2).
- Strobach, E. J., 2022: A single column model evaluation of mixing length formulations and constraints for the sa-TKE-EDMF planetary boundary layer parameterization. *Wea. Forecasting*, <https://doi.org/10.1175/WAF-D-21-0059.1>, in press.

- Stull, R. B., 1976: The energetics of entrainment across a density interface. *J. Atmos. Sci.*, **33**, 1260–1267, [https://doi.org/10.1175/1520-0469\(1976\)033<1260:TEOEAD>2.0.CO;2](https://doi.org/10.1175/1520-0469(1976)033<1260:TEOEAD>2.0.CO;2).
- , 1988: *An Introduction to Boundary Layer Meteorology*. Kluwer Academic, 666 pp.
- Vogelezang, D. H. P., and A. A. M. Holtslag, 1996: Evaluation and model impacts of alternative boundary-layer height formulations. *Bound.-Layer Meteor.*, **81**, 245–269, <https://doi.org/10.1007/BF02430331>.
- Wang, Y., B. Jia, S.-C. Wang, M. Estes, L. Shen, and Y. Xie, 2016: Influence of the Bermuda high on interannual variability of summertime ozone in the Houston–Galveston–Brazoria region. *Atmos. Chem. Phys.*, **16**, 15 265–15 276, <https://doi.org/10.5194/acp-16-15265-2016>.
- Wei, P., S. Cheng, J. Li, and F. Su, 2011: Impact of boundary-layer anticyclonic weather system on regional air quality. *Atmos. Environ.*, **45**, 2453–2463, <https://doi.org/10.1016/j.atmosenv.2011.01.045>.
- Wernli, H., 1997: A Lagrangian-based analysis of extratropical cyclones. I: A detailed case-study. *Quart. J. Roy. Meteor. Soc.*, **123**, 1677–1706, <https://doi.org/10.1002/qj.49712354211>.
- Wilczak, J. M., E. E. Gossard, W. D. Neff, and W. L. Ebrehard, 1996: Ground based remote sensing of the atmospheric boundary layer: 25 years of progress. *Bound.-Layer Meteor.*, **71**, 321–349, https://doi.org/10.1007/978-94-017-0944-6_14.
- Winkler, J. A., B. R. Skeeter, and P. D. Yamamoto, 1988: Seasonal variations in the diurnal characteristics of heavy hourly precipitation across the United States. *Mon. Wea. Rev.*, **116**, 1641–1658, [https://doi.org/10.1175/1520-0493\(1988\)116<1641:SVITDC>2.0.CO;2](https://doi.org/10.1175/1520-0493(1988)116<1641:SVITDC>2.0.CO;2).
- Wulfmeyer, V. O., and T. Janjić, 2005: Twenty-four-hour observations of the marine boundary layer using shipborne NOAA high-resolution Doppler lidar. *J. Appl. Meteor.*, **44**, 1723–1744, <https://doi.org/10.1175/JAM2296.1>.
- Yi, C., K. J. Davis, B. W. Berger, and P. S. Bakwin, 2001: Long-term observations of the dynamics of the continental planetary boundary layer. *J. Atmos. Sci.*, **58**, 1288–1299, [https://doi.org/10.1175/1520-0469\(2001\)058<1288:LTOOTD>2.0.CO;2](https://doi.org/10.1175/1520-0469(2001)058<1288:LTOOTD>2.0.CO;2).
- Zhang, Y., D. J. Seidel, and S. Zhang, 2013: Trends in planetary boundary layer height over Europe. *J. Climate*, **26**, 10 071–10 076, <https://doi.org/10.1175/JCLI-D-13-00108.1>.